Inorganica Chimica Acta 579 (2025) 122553

Contents lists available at ScienceDirect

Inorganica Chimica Acta

journal homepage: www.elsevier.com/locate/ica

Research paper

Hydrophobic gold nanoparticles coupled with fluorescent dyes: A smart tool for optoelectronic applications☆

Sara Cerra [a,*], Damiano Cirri [b], Chiara Gabbiani [b], Alessandro Pratesi [b], Souren Grigorian [c], Roberto Matassa [d,e], Juan G. Lozano [f], Ana M. Beltrán [f], Angela Capocefalo [g], Claudia Fasolato [h], Francesca A. Scaramuzzo [i], Martina Marsotto [j], Chiara Battocchio [k], Tommaso A. Salamone [a], Beatrice Pennacchi [a], Martina Mercurio [a], Ilaria Fratoddi [a,l,m,*]

[a] Department of Chemistry, Sapienza University of Rome, P.le Aldo Moro 5 00185 Rome, Italy
[b] Department of Chemistry and Industrial Chemistry (DCCI), University of Pisa, Via Moruzzi 13 56124 Pisa, Italy
[c] Institute of Physics, University of Siegen, Walter-Flex-Strasse 3 D-57068 Siegen, Germany
[d] Physics Division, School of Science and Technology, University of Camerino 62032 Camerino, MC, Italy
[e] Department of Anatomical, Histological, Forensic and Orthopaedic Sciences, Section of Human Anatomy, Sapienza University of Rome, Via A. Borelli 50, 00161 Rome, Italy
[f] Departamento de Ingeniería y Ciencia de los Materiales y del Transporte, Escuela Técnica Superior de Ingeniería y Escuela Politécnica Superior, Universidad de Sevilla, 41092 Seville, Spain
[g] Department of Physical and Chemical Sciences, University of L'Aquila, Via Vetoio, Coppito 67100 L'Aquila, Italy
[h] CNR-ISC, Institute for Complex Systems, National Research Council, c/o Sapienza University of Rome, P.le A. Moro 5, 00185 Rome, Italy
[i] Department of Basic and Applied Sciences for Engineering (SBAI), Sapienza University of Rome, Via A. Scarpa 14, 00161 Rome, Italy
[j] Department of Chemical Science and Technologies, Tor Vergata University of Rome, Via della Ricerca Scientifica 1, 00133 Rome, Italy
[k] Department of Sciences, Roma Tre University, Via della Vasca Navale 79, 00146 Rome, Italy
[l] Research Center for Applied Sciences to the Safeguard of Environment and Cultural Heritage (CIABC), Sapienza University of Rome, Piazzale Aldo Moro 5, 00185 Rome, Italy
[m] Research Center for Nanotechnology Applied to Engineering of Sapienza (CNIS), Sapienza University of Rome, Piazzale Aldo Moro 5, 00185 Rome, Italy

ARTICLE INFO

Keywords:
Gold nanoparticles
Organic thiols
Fluorescent dyes
Photoluminescence
Nanocomposites
Electrical measurements
Optoelectronics

ABSTRACT

In this work, gold nanoparticles (AuNPs) are functionalized with two different rigid, conjugated thiol ligands: (i) 9,9-didodecyl-2,7-bis(acetylthio)fluorene (FL) and (ii) 2-(anthracen-9-ylmethyl)thio)ethane-1-thiol (2AET). Functionalized AuNPs synthesis is carried out *via* a two-phase wet chemical reduction method, using $NaBH_4$ as a reducing agent. During the synthesis procedure, ligands are used in 2AET/FL mixture exploring different molar ratios. On freshly prepared samples, UV–Vis and DLS studies demonstrate the reproducibility of the synthesis method over the molar ratios investigated, with the 2AET/FL 1:2 molar ratio giving the most stable colloids up to one year of aging. Infrared spectroscopies (FTIR, Far-IR) and SR-XPS allow a deep surface AuNPs characterization, which show tunable photoluminescence upon excitation by different wavelengths. To exploit potential optoelectronic applications, the π-conjugated polymer poly(phenylacetylene) (PPA) is used to prepare nanocomposites with different AuNPs/PPA weight ratios (from 10/90 to 90/10 %wt.). Morphological studies carried out with AFM and HR-TEM show 4 nm quasi-spherical shape AuNPs uniformly blended within the polymer. The electric response is assessed onto spin-coated thin films (thickness ca. 4 nm). At the highest AuNPs amount, the band gap is reduced up to 2.15 eV with an increase in the electrical conductivity of about 2.5 times compared with AuNPs and PPA.

1. Introduction

The design of metal nanostructures functionalized with fluorescent ligands without expensive fabrication facilities is rapidly emerging at the research frontier to confer additional and novel optoelectronic properties to nanomaterials. In the nanoscale size range (1–100 nm),

☆ This article is part of a special issue entitled: 'Alberto Albinati' published in Inorganica Chimica Acta.

* Corresponding authors at: Department of Chemistry, Sapienza University of Rome, P.le Aldo Moro 5, 00185 Rome, Italy (I. Fratoddi and S. Cerra).
E-mail addresses: sara.cerra@uniroma1.it (S. Cerra), ilaria.fratoddi@uniroma1.it (I. Fratoddi).

https://doi.org/10.1016/j.ica.2025.122553
Received 20 September 2024; Received in revised form 14 January 2025; Accepted 16 January 2025
Available online 23 January 2025

noble metal nanoparticles (Au-, Ag-, PdNPs) show exotic physicochemical properties due to their quantum confinement and high surface-*to*-volume ratio [1–3]. Concerning this category, gold nanoparticles (AuNPs) are one of the most explored due to their oxidation resistance, surface chemical versatility, and unique optical properties, such as the localized surface plasmon resonance (SPR) ascribable to the collective oscillating surface electrons (*i.e.*, plasmons) associated to the strong optical extinction band (500–600 nm) [4]. However, intrinsic photoluminescent behavior pertains only to ultrasmall gold nanocrystals consisting of several to tens of metal atoms, whose size is comparable to the Fermi wavelength of the electron (ca. 1 nm) [4]. Nanoparticle size influences the fluorescence, which is only observed for spherical AuNPs with a diameter $\leq$10 nm (rationalized from a dipole-induced non-radiative energy transfer), whereas for large nanoparticles (>10 nm), quenching always dominates [5,6]. Yet from optical and surface-related perspectives, recent publications reported on the surface functionalization of gold nanoparticles with organic fluorescent dyes [7–9]. Surface modification of AuNPs using dyes also overcomes typical limitations of organic molecules such as photobleaching (fluorescence intensity decrease in time and/or shift of their absorption/emission spectra), widening the range of applications (organic solar cells, photocatalysis, photonic devices, and optically responsive materials) [10,11]. Different synthesis strategies have been adopted to obtain stable, dye-functionalized AuNPs, both covalent and non-covalent, using rhodamine and fluorescein-based molecules [12–14]. The reported studies clearly highlight that the fine tuning of fluorescence is possible according to dye concentration [12], AuNPs size [13], and shape [13]. In particular, Kumar et al. [12] showed that the dye concentration on AuNPs has a pronounced influence on the absorption and emission behavior of dye-functionalized AuNPs. Fratoddi et al. [14] were able to modulate both the amount of dye capping agent (rhodamine 6G isothiocyanate) covalently linked on AuNPs and their dielectric constant, by tuning the plasmon resonance over a large range of wavelengths. However, the interaction of dye molecules with plasmonic surfaces may also generate quenching/superquenching mechanisms (effective energy transfer) when overlapping of spectral donor–acceptor absorptions occurs [13]. Reasonably, in the case of AuNPs (SPR 500–600 nm), quenching of fluorescence efficiency and lifetime mainly concerns dyes with absorption/emission in the visible spectral region, also depending on the separation distance between the fluorophore and the AuNPs surface [12]. Therefore, a critical remark concerns the stabilization of AuNPs against irreversible aggregation, which induces a decrease in surface energy, fluorophore lifetime, and efficiency. The most effective stabilization strategy is the covalent functionalization of AuNPs with thiols/thiolated molecules, taking advantage of the high chemical affinity between gold and sulphur [15]. Current research focuses on the synthesis of multifunctional nanoparticles, able to combine more than one physicochemical property on the same nanoplatform [16]. However, only a few studies exploit the possibility of a mixed functionalization to have both synergistic fluorescent and electrical properties, taking advantage of the interparticle near-field coupling effect [17].

Bearing this in mind, in this work we synthesized organic soluble AuNPs functionalized with two different organic, π-conjugated synthetic thiols, *i.e.*, 9,9-didodecyl-2,7-bis(acetylthio)fluorene (FL) and 2-(anthracen-9-ylmethyl)thio)ethane-1-thiol (2AET), both bearing an activable thiolate group (–SH or –$SCOCH_3$), which can be exploited for covalent binding with the gold surface. Attention has been given to optimizing synthesis conditions for mixed functionalized gold nanoparticles, namely AuNPs-2AET-FL_1 (molar ratio 2AET:FL 1:1), AuNPs-2AET-FL_2 (molar ratio 2AET:FL 1:2), and AuNPs-2AET-FL_4 (molar ratio 2AET:FL 1:4). The fluorene derivative was chosen due to its fluorescence in the 300–400 nm range with negligible quenching effect after AuNPs conjugation and its proven conductivity enhancement when used in polymer blends [18]. Fluorescent 2AET with its anthracene moiety has been designed to exploit an electron-rich structure with absorption/emission not overlapping with the typical SPR band of AuNPs, thus showing optically active behavior in the near-UV region. With potential applications in optoelectronics, AuNPs-2AET-FL_2 has been used as inorganic fillers in a semiconducting poly(phenylacetylene) (PPA) matrix at different weight ratios (from 10/90 to 90/10 AuNPs/PPA %wt.) to obtain hybrid organic/inorganic nanocomposites *via* simple blending approach at room temperature. Compared with pristine AuNPs, nanocomposite arrangement is more prone to applications in miniaturized, flexible devices [19]. PPA has been chosen as a π-conjugated model polymer in the nanocomposite architecture due to its dynamic helical structure, opening the possibility for preparing materials with combined fluorescent-electrical and potential dynamic chiral plasmon response [20]. To obtain insight into the structural and optical behavior of these colloidal nanoparticles and nanocomposites, a combination of characterization techniques has been exploited. UV–Vis and photoluminescence (PL) assessed their optical properties. Infrared spectroscopy (FTIR, Far-IR) and synchrotron radiation-induced X-ray photoelectron spectroscopy (SR-XPS) were employed for extensive structural characterization, whereas, at solid-state, morpho-structural analyses have been carried out using atomic force microscopy (AFM), and high-resolution transmission electron microscopy (HR-TEM). In organic solvent suspension, the hydrodynamic diameter value ($<2R_H>$) has been estimated by dynamic light scattering (DLS). The electrical response of both pristine gold nanoparticles and nanocomposites was evaluated *via* electrical (I/V) measurements in the form of spin-coated thin films onto interdigitated ITO electrodes.

2. Experimental section

2.1. Materials

Tetrachloroauric(III) acid trihydrate ($HAuCl_4$, 99.0 %, M.W. 393.83 g/mol), tetraoctylammonium bromide (TOAB, $(CH_3(CH_2)_7)_4N^+Br^-$, 98 %, M.W. 546.79 g/mol), sodium borohydride ($NaBH_4$, ≥98.0 %, M.W. 37.83 g/mol), 9,9-didodecyl-2,7-dibromofluorene (FL-Br, $C_{37}H_{56}Br_2$, 97.0 %, M.W. 660.65 g/mol), sodium methanethiolate (CH_3SNa, ≥90.0 %, M.W. 70.09 g/mol), dimethylformamide (C_3H_7NO, DMF, anhydrous, M.W. 73.10 g/mol), 1,2-ethanedithiol ($C_2H_6S_2$, 98 %, 94.20 g/mol), potassium carbonate (K_2CO_3, 99 %, 138.21 g/mol), 9-chloromethylanthracene ($C_{15}H_{11}Cl$, 99 %, 226.70 g/mol). Previously synthetized stereoregular *cis*-transoid poly(phenylacetylene) (PPA) was used [21]. 1,3-Dimethyl-2-imidazolidinone (DMI, $C_5H_{10}N_2O$, ≥99.5 %, M.W. 114.15 g/mol), acetyl chloride (CH_3COCl, ≥99.0 %, M.W. 78.50 g/mol), petroleum ether (40–60 °C, ≥ 90 %), diethyl ether ($C_2H_{10}O$, 99 %, 74.12 g/mol), *n*-pentane (C_5H_{12}, 99 %, 72.15 g/mol), dichloromethane (DCM, CH_2Cl_2, ≥99.9 %), chloroform ($CHCl_3$, ≥99.5 %), toluene ($C_6H_5CH_3$, ≥99.5 %), ethanol (CH_3CH_2OH, 96 %), and isopropyl alcohol (i-PrOH, $(CH_3)_2CHOH$, ≥99.8 %) were all Merck (Milan, Italy) and used without further purification. Ultrapure water (H_2O_{up}, 18.3 MΩ·cm) produced with a Zeneer Power I Scholar-UV water purification system (Fulltech Instruments, Rome, Italy) was used in all aqueous solutions. A high-speed micro-centrifuge (Scilogex, Rocky Hill, Connecticut, USA) was used for purification of the colloidal suspensions. Thin-layer chromatography (TLC) separation was performed on silica gel (TLC-PET foils) with fluorescent indicator 254 nm (Merck, Milan, Italy).

2.2. Methods

2.2.1. Synthesis of 2-((anthracen-9-ylmethyl)thio)ethane-1-thiol (2AET)

In a 100 mL flask were added 10 mL of anhydrous DMF, 2.7 g of K_2CO_3 and 5 mL of 1,2-ethanedithiol. The mixture was stirred at room temperature and a solution of 2.0 g of 9-chloromethylanthracene in 25 mL of DMF was added through a dropping funnel apparatus in about 5 h. The resulting mixture was stirred at room temperature overnight, then the solvent was removed through a rotary evaporator. The crude product was washed in a Hirsch funnel with a few mL of a cold 1:1 v/v mixture of diethyl ether and *n*-pentane and dried in a desiccator through

a high vacuum pump. After desiccation the 2.5 g of yellow solid were obtained. The crude reaction product was analyzed through ^{1}H NMR and was found to be a 2:1 mixture of the expected product, together with the dialkylated counterpart (R—S—CH_2CH_2—S—R, R=$C_{15}H_{11}$) as a contaminant. Since in the following experimental steps the contaminant was not reactive, the crude product was employed without further purifications. The contaminant was finally removed during the nanoparticles centrifugation steps (see paragraph 2.2.2). Full characterizations are reported in Fig. S1 in the Supporting Information.

Physical properties and spectral data of 2AET: UV–vis (CH_2Cl_2): λ = 321, 337, 354, 372 (max), 393 nm; PL (CH_2Cl_2): λ_{ex} = 375 nm, λ_{em} = 400, 420 (max), 444 nm; ^{1}H NMR (400 MHz, $CDCl_3$, δ): 8.41 (m, 1H, Ar H), 8.32 (m, 2H, Ar H), 8.00 (m, 4H, Ar H), 7.40–7.60 (m, 4H, Ar H), 4.78 (m, 2H, CH_2), 2.86 (m, 2H; CH_2), 2.77 (m, 2H; CH_2), 1.80 (broad, 1H; SH); FT-IR (KRS-5) [22,23]: ν = 3309 (w; —OH)), 3048 (w, (—CH) aromatic), 2917 (m; ν_{as}(—CH_2)), 2876 (m; ν_s(—CH_2)), 2562 (w; ν(—SH)), 1670 (s; ν(CC) Ar), 1595 (s; ν(CC) Ar), 1481 (w; ν(CC) Ar), 1445 (m; δ_s(—CH_2)), 1411 (m; δ(—CH_3), γ(—CH_2)), 1282 (m; ν_{as}(C—C—C), 1035 (s; *in-plane* δ(=CH)), 885 (s; def. modes (CC) Ar), 795 (m; def. modes (CC) Ar), 731 (s, *out-of-plane* δ(—CH) Ar), 643 (w, ν(C—S)); Far-IR (PE) [24–26]: ν = 566 (w; *in-plane* ring deformation mode), 523 (m; *out-of-plane* ring deformation), 472 (w; *in-plane* ring deformation mode) 405 (m; *out-of-plane* C—C deformation), 386 ρ(—CH_2), 302 (m; —S—C—C deformation), 286 (w, ρ(—CH_2)), 253 (w, ρ(—CH_2)), 225 (w, ρ(—CH_2)). HRMS (ESI) *m/z*: $[M+H]^+$ calcd. for $C_{17}H_{15}S_2$, 283.0615; found, 283.0602 (mass error: −4.6 ppm).

N.B. The species identified by ESI-MS analysis apparently differs from the desired compound. This behavior can be easily explained taking into account that oxidized species can be formed during the ionization process [27].

2.2.2. Synthesis of gold nanoparticles stabilized with 2AET and FL ligands

Synthesis of the fluorene derivative was carried out by optimizing a previously reported protocol [3]. A detailed procedure together with main characterizations are reported in the Supporting Information and Fig. S2. Hydrophobic gold nanoparticles were synthesized using a modified two-phase Brust-Shiffrin procedure [28]. $HAuCl_4$ (0.0500 g, $1.27{\cdot}10^{-4}$ mol) was dissolved in 5 mL of H_2O_{up} and mixed with 0.0694 g of TOAB as phase-transfer agent solubilized in 5 mL of toluene ($HAuCl_4$:TOAB 1:1 mol/mol). The aqueous/toluene mixture was stirred for 5 min to allow the complete transfer of $[(CH_3(CH_2)_7)_4N]^+$ $[AuCl_4]^-$ complex in the organic phase. Then, the FL thioacetate ligand and the 2AET dye were dissolved in 5 mL of toluene (each) and added to the reaction mixture with different molar ratios between reagents $HAuCl_4$/2AET/FL: 1:0.5:0.5 (AuNPs-2AET-FL_1), 1:0.5:1 (AuNPs-2AET-FL_2), and 1:0.5:2 (AuNPs-2AET-FL_4). The reaction was degassed under Ar flux for 15 min, and 0.0480 g of $NaBH_4$ ($1.27{\cdot}10^{-3}$ mol, $HAuCl_4$:$NaBH_4$ 1:10 mol/mol) in 5 mL of H_2O_{up} were injected dropwise with a syringe to achieve gold precursor reduction in the presence of thiols as functionalizing agents. The synthesis mixture was vigorously stirred for 3 h at room temperature, turning from orange to dark brown. In the end, the crude mixture was transferred into a separatory funnel and repeatedly washed with brine (5 × ca. 10 mL). The organic phase was separated and removed by a rotary evaporator. The as-synthesized thiol-functionalized AuNPs were recovered with 20 mL of ethanol, split into centrifuge tubes, and purified by repeated centrifuges (4×, 10 000 rpm, 9503 g, 10 min, +8 °C). After purification steps, ethanol was removed under reduced pressure, and nanoparticles were redispersed in CH_2Cl_2 for further use.

Physical properties and spectral data of AuNPs-2AET-FL_1. UV–Vis (CH_2Cl_2): λ_{SPR} = 533 nm (fresh), 630 nm (aged, 1 year); PL (CH_2Cl_2): λ_{ex} = 333 nm, λ_{em} = 362, 395, 418 (max), 440 nm, λ_{ex} = 370 nm, λ_{em} = 398, 418 (max), 440 nm; FT-IR (KRS-5): ν = 3061 (w, (—CH) aromatic), 2955 (w; ν_{as}(—CH_2)), 2926 (s; ν_{as}(—CH_2)), 2852 (m; ν_s(—CH_2)), 1731 (m; ν(C=O)), 1671 (m; ν(CC) Ar), 1592 (m; ν(CC) Ar), 1490 (w; ν(CC) Ar), 1461 (s; δ_s(—CH_2)), 1406 (w; δ(—CH_3), γ(—CH_2)), 1377 (w; δ(—CH_3), γ(—CH_2)), 1262 (m; ν_{as}(C—C—C), 1095 (m; *in-plane* δ(=CH)), 1032 (s; *in-plane* δ(=CH)), 886 (w; def. modes (CC) Ar), 807 (s; def. modes (CC) Ar), 733 (m, *out-of-plane* δ(—CH) Ar), 663 (w, ν(C—S)); 616 (w, ν(=C—S)); Far-IR (PE, i-PrOH): ν = 590 (w; *in-plane* ring deformation mode), 521 (w; *out-of-plane* ring deformation), 485 (w; *in-plane* ring deformation mode), 415 (w; *out-of-plane* C—C deformation), 377 (w, ρ(—CH_2)), 326 (w; ring *in-plane* bending), 309 (w, —S—C—C deformation), 280 (m; ρ(—CH_2)), 243 (m; ν(Au—S)); <$2R_H$> (DLS, CH_2Cl_2): (12 ± 2) nm; (60 ± 25) nm; (185 ± 65) nm; yield: 34 %w/w. Yield was calculated as gold nanoparticles/gold precursor weight ratio.

Physical properties and spectral data of AuNPs-2AET-FL_2. UV–Vis (CH_2Cl_2): λ_{SPR} = 533 nm (fresh), 545 nm (aged, 1 year); PL (CH_2Cl_2): λ_{ex} = 333 nm, λ_{em} = 345, 362 (max), 377, 408 (tail) nm, λ_{ex} = 370 nm, λ_{em} = 394, 415 (max), 440 nm; FT-IR (KRS-5): ν = 3061 (w, (—CH) aromatic), 2955 (w; ν_{as}(—CH_2)), 2926 (s; ν_{as}(—CH_2)), 2852 (m; ν_s(—CH_2)), 1710 (m; ν(C=O)), 1663 (m; ν(CC) Ar), 1594 (m; ν(CC) Ar), 1482 (w; ν(CC) Ar), 1465 (s; δ_s(—CH_2)), 1403 (w; δ(—CH_3), γ(—CH_2)), 1381 (w; δ(—CH_3), γ(—CH_2)), 1260 (m; ν_{as}(C—C—C), 1093 (m; *in-plane* δ(=CH)), 1020 (s; *in-plane* δ(=CH)), 880 (w; def. modes (CC) Ar), 805 (m; def. modes (CC) Ar), 735 (w, *out-of-plane* δ(—CH) Ar), 654 (w, ν(C—S)); 613 (w, ν(=C—S)); Far-IR (PE, i-PrOH): ν = 587 (w; *in-plane* ring deformation mode), 523 (w; *out-of-plane* ring deformation), 477 (w; *in-plane* ring deformation mode), 385 (w, ρ(—CH_2)), 326 (w; ring *in-plane* bending), 288 (w; ρ(—CH_2)), 242 (m; ν(Au—S)); <$2R_H$> (DLS, CH_2Cl_2): (30 ± 5) nm; (68 ± 15) nm; (260 ± 70) nm; yield: 34 %wt. Yield was calculated as gold nanoparticles/gold precursor weight ratio.

Physical properties and spectral data of AuNPs-2AET-FL_4. UV–Vis (CH_2Cl_2): λ_{SPR} = 533 nm (fresh), 620 nm (aged, 1 year); PL (CH_2Cl_2): λ_{ex} = 333 nm, λ_{em} = 345, 362 (max), 377, 408 (tail) nm, λ_{ex} = 370 nm, λ_{em} = 394, 415 (max), 440 nm; FT-IR (KRS-5): ν = 3058 (w, (—CH) aromatic), 2955 (w; ν_{as}(—CH_2)), 2926 (s; ν_{as}(—CH_2)), 2852 (m; ν_s(—CH_2)), 1732 (m; ν(C=O)), 1669 (m; ν(CC) Ar), 1595 (m; ν(CC) Ar), 1490 (w; ν(CC) Ar), 1461 (s; δ_s(—CH_2)), 1404 (w; δ(—CH_3), γ(—CH_2)), 1377 (w; δ(—CH_3), γ(—CH_2)), 1260 (m; ν_{as}(C—C—C), 1099 (m; *in-plane* δ(=CH)), 1032 (s; *in-plane* δ(=CH)), 883 (w; def. modes (CC) Ar), 805 (s; def. modes (CC) Ar), 730 (m, *out-of-plane* δ(—CH) Ar), 661 (w, ν(C—S)); 605 (w, ν(=C—S)); Far-IR (PE, i-PrOH): ν = 573 (w; *in-plane* ring deformation mode), 539 (w; *out-of-plane* ring deformation), 482 (w; *in-plane* ring deformation mode), 326 (w; ring *in-plane* bending), 309 (w, —S—C—C deformation), 278 (w; ρ(–CH_2)), 241 (m; ν(Au–S)); <$2R_H$> (DLS, CH_2Cl_2): (3 ± 1) nm; (37 ± 5) nm; (205 ± 30) nm; yield: 20 %w/w. Yield was calculated as gold nanoparticles/gold precursor weight ratio.

2.2.3. Gold nanoparticles/poly(phenylacetylene) nanocomposite blend synthesis

Gold nanoparticles/poly(phenylacetylene) (AuNPs/PPA) nanocomposite material was synthesized following a single-step blending approach at room temperature. A 2 mg/mL of PPA solution and a 2 mg/mL of AuNPs suspension in $CHCl_3$ were used as stock solutions for the preparation of 2 mL of nanocomposites with different AuNPs/PPA weight ratios (%wt.): 10/90, 30/70, 50/50, 70/30, 90/10. The mixture was gently stirred for 3 h at room temperature under Ar atmosphere. Then, the final blend was stored for further use at +4 °C under inert atmosphere.

2.2.4. Sample characterization

UV–visible spectroscopy. UV–Visible spectra were acquired on a Varian Cary 100 spectrophotometer in the 200–800 nm wavelength range. Quartz cells having an optical path length of 1 cm were used using $CHCl_3$ or CH_2Cl_2 as solvents.

Photoluminescence spectroscopy. Steady-state emission spectra were recorded on a PerkinElmer LS50 luminescence spectrometer using a quartz cuvette with a 1 mm optical path for the excitation. Monochromator slits resolution was set at 2.5 nm for both excitation and emission. Excitation wavelength was set according to the UV–Vis absorption maxima for each sample, using CH_2Cl_2 as solvent.

Fourier-transform infrared spectroscopy. FT-IR and Far-IR spectra were

acquired with a Bruker Vertex 70 instrument in the spectral range 4000–400 cm^{-1} and 600–200 cm^{-1}, respectively. FT-IR samples were deposited as a thin drop casted film on KRS-5 cells (transparency range 4000–400 cm^{-1}) from their $CHCl_3$ or CH_2Cl_2 suspensions. Far-IR analysis was performed by depositing the samples onto polyethylene windows (transparency range from 500 to >100 cm^{-1}) [29] from i-PrOH suspensions. The resolution was 4 cm^{-1} with a minimum of 32 scans.

Nuclear Magnetic Resonance. Monodimensional ^1H NMR spectra were recorded on a Bruker Avance III operating at 400 MHz for the proton (298 K). Reagents and precursors spectra were acquired with a spectral width of 15 ppm (9013.7 Hz), 64 k data points and 16 scans. The recycle delay was set to 6.55 s to achieve complete resonance relaxation between successive scansions. Residual ^1H resonance from the deuterated solvent ($CDCl_3$, $\delta = 7.26$ ppm) is used to reference the ^1H spectrum. Chemical shift values were given in parts per million (δ, ppm).

ESI-MS spectroscopy. High-resolution ESI mass spectrum for 2AET was recorded by direct injection at 3 μL/min flow rate in a Thermo-Fisher Q Exactive Plus Orbitrap mass spectrometer, equipped with an ionization electrospray (ESI) source and a hybrid-quadrupole analyzer working at nominal resolution (at *m/z* 400) of 100,000.

The experimental conditions were as follows: positive polarity, spray voltage 3.1 kV, capillary voltage 45 V, capillary temperature 220 °C, tube lens voltage 230 V. The sheath and the auxiliary gases were set at 17 and 1 (arbitrary units), respectively. For acquisition, Xcalibur 2.0. software (Thermo) was used.

Dynamic Light Scattering. The intensity-weighted distribution of hydrodynamic diameters ($<2R_H>$) of AuNPs $CHCl_3$ suspensions was measured by dynamic light scattering (DLS) on a Malvern Zetasizer Nano ZS90 instrument at 25 °C using a 4 mW laser light with the wavelength of 632.8 nm. Measurements were done with a minimum of three replicates and reported as mean ± standard deviation.

Spin coater. AuNPs/PPA nanocomposite blends were deposited onto Si/SiO_2 glass substrates or onto interdigitated ITO substrates using Electron MEC PRS 5 V Spinner at room temperature. Parameters were: speed 600 rpm, 1 min.

Atomic Force Microscopy. AFM was performed on a Veeco AFM Multimode equipped with Nanoscope IIIa on spin-coated samples on glass substrates, from CH_2Cl_2 suspensions. The measurements were acquired in tapping mode using RTESP Bruker tips (nominal parameters r = 8 nm, f = 300 kHz, k = 40 N/m) with a 512 × 512 pixels resolution. Post-capture correction by polynomial background filters and analysis was performed by using the software Gwyddion 2.56.

Synchrotron radiation (SR)-induced X-ray Photoelectron Spectroscopy. SR-XPS experiments were carried out on cast deposited films on Titania substrates, at the materials science beamline (MSB) at the Elettra synchrotron radiation source (Trieste, Italy). MSB is placed at the left end of the bending magnet 6.1 and it is equipped with a plane grating monochromator that provides light in the energy range of 21–1000 eV. The base pressure in the UHV end station is of 2×10^{-10} mbar; the end station is equipped with a SPECS PHOIBOS 150 hemispherical electron analyzer; low-energy electron diffraction optics; a dual-anode Mg/Al X-ray source; an ion gun; a sample manipulator with a K-type thermocouple attached to the rear side of the sample. For these experiments, we detected photoelectrons emitted by C1s, S2p and Au4f core levels at normal emission geometry. Calibration of the energy scale was made referencing the spectra to the C1s core level signal of aromatic C atoms, fixed at 284.7 eV. Curve-fitting analysis of the spectra was done using Gaussian curves as fitting functions, after the subtraction of a polynomial background. The $S2p_{3/2,1/2}$ doublets were fitted using the same full width at half-maximum (FWHM) for both components, a spin–orbit splitting of 1.2 eV and a branching ratio ($2p_{3/2}/2p_{1/2}$) of 2. The $Au4f_{7/2,5/2}$ doublets were fitted using the same full width at half-maximum (FWHM) for both components, a spin–orbit splitting of 3.7 eV and a branching ratio ($4f_{7/2}/4f_{5/2}$) of 4/3. When several different species were identified in a spectrum, the same FWHM value was set for all individual photoemission bands.

High-resolution Transmission Electron Microscopy. HR-TEM images were acquired using FEI Talos F200S Field Emission Gun (FEG) microscope operating at 200 keV on samples deposited on Ni-support grid coated with a carbon amorphous film. Energy dispersive X-ray spectroscopy (EDX) compositional analysis maps were collected using a Super-X energy dispersive X-ray spectrometry system which includes two silicon drift detectors, coupled to the microscope in the Scanning Transmission Electron Microscopy (STEM) mode, using spatial drift correction and a dwell time of 0.2 s.

Electrical measurements. The current/voltage characterization of the samples was carried out on a Keithley 595 CVmeter equipped with an Ossila low density OFET test board unit in the ±20 V voltage range (V step 0.5 V). 100 μL of samples were deposited by spin coating onto pre-patterned Ossila interdigitated ITO substrates (20 × 15 mm, resistance 20 Ω/square, ITO thickness 100 nm) with five OFETs with individual source-drain connections (channel dimensions W × L: 30 mm × 50 μm). Tests were performed at room temperature and in the visible light.

3. Results and discussion

3.1. Synthesis and spectroscopic characterization of functionalized gold nanoparticles

Gold nanoparticles stabilized with mixed rigid, π-conjugated, fluorescent ligands, *i.e.* 2AET and FL thioacetate in different 2AET/FL molar ratios (1:1, 1:2, 1:4, namely AuNPs-2AET-FL_1, AuNPs-2AET-FL_2, and AuNPs-2AET-FL_4, respectively) were synthesized under optimized conditions according to a modified Brust-Schiffrin method [3]. It is noteworthy that the FL ligand bears two thiol-ending groups, and it is a suitable linker for the formation of interconnected nanoparticles, leading to super-aggregates. The synthesis procedure is schematized in Fig. 1a. After the purification steps, the formation of colloidal thiol-functionalized AuNPs-2AET-FL was confirmed by the appearance of the characteristic SPR absorption band centered at 533 nm (Fig. 1b). The shape of the SPR band reflects the morphology of nanoparticles and the presence of a single absorption maximum suggested the formation of spherical nanoparticles [30]. Importantly, a further absorption band in the 300–400 nm range was detected, associated with the presence of 2AET dye on AuNPs surface, partially overlapping with that of FL ligand at 318 nm. An estimation of the relative quantity of the thiol ligands on each colloidal freshly prepared AuNPs can be extrapolated from the UV–Vis considering the following ratio (*Q*, Eq. (1)):

$$Q = \frac{Abs_{peak}}{Abs_{372\,nm}} \quad (1)$$

where Abs_{peak} is the wavelength at the maximum absorption of FL (λ_{max} = 318) or at the λ_{SPR} = 533 nm, respectively. The ratio considers the normalization to maximum absorption of 2AET dye (λ_{max} = 372 nm), since its quantity is fixed in the synthesis protocol. For AuNPs-2AET-FL_1 calculated *Q* between 2AET/FL gave a 1:1.02 absorbance ratio with a AuNPs/thiols 0.54:1, for AuNPs-2AET-FL_2, 2AET/FL *Q* value was 1:0.98 and AuNPs/thiols 0.54:1, whereas for AuNPs-2AET-FL_4 *Q* between 2AET/FL was 1:1.03 and AuNPs/thiols 0.46:1. These results evidenced that, for the molar ratios herein explored, a 1:1 ratio between ligands is maintained through samples, although in the case of AuNPs-2AET-FL_4 a low AuNPs yield was obtained. In all cases, AuNPs showed a single, broad plasmon band, with a calculated full-width-at-half-maximum (FWHM) value of (205 ± 1) nm. The FWHM value (or SPR peak width) is known to depend on the size distribution of colloidal nanoparticles but also on the coupling effect between gold cores in the case of close or interconnected AuNPs [31,32].

A more accurate evaluation of the super-aggregates size in colloidal suspension was obtained from dynamic light scattering (DLS) analysis. Intensity-weighted hydrodynamic diameter distributions of AuNPs are reported in Fig. 1c. For AuNPs-2AET-FL_1 (Fig. 1c, dark cyan trace),

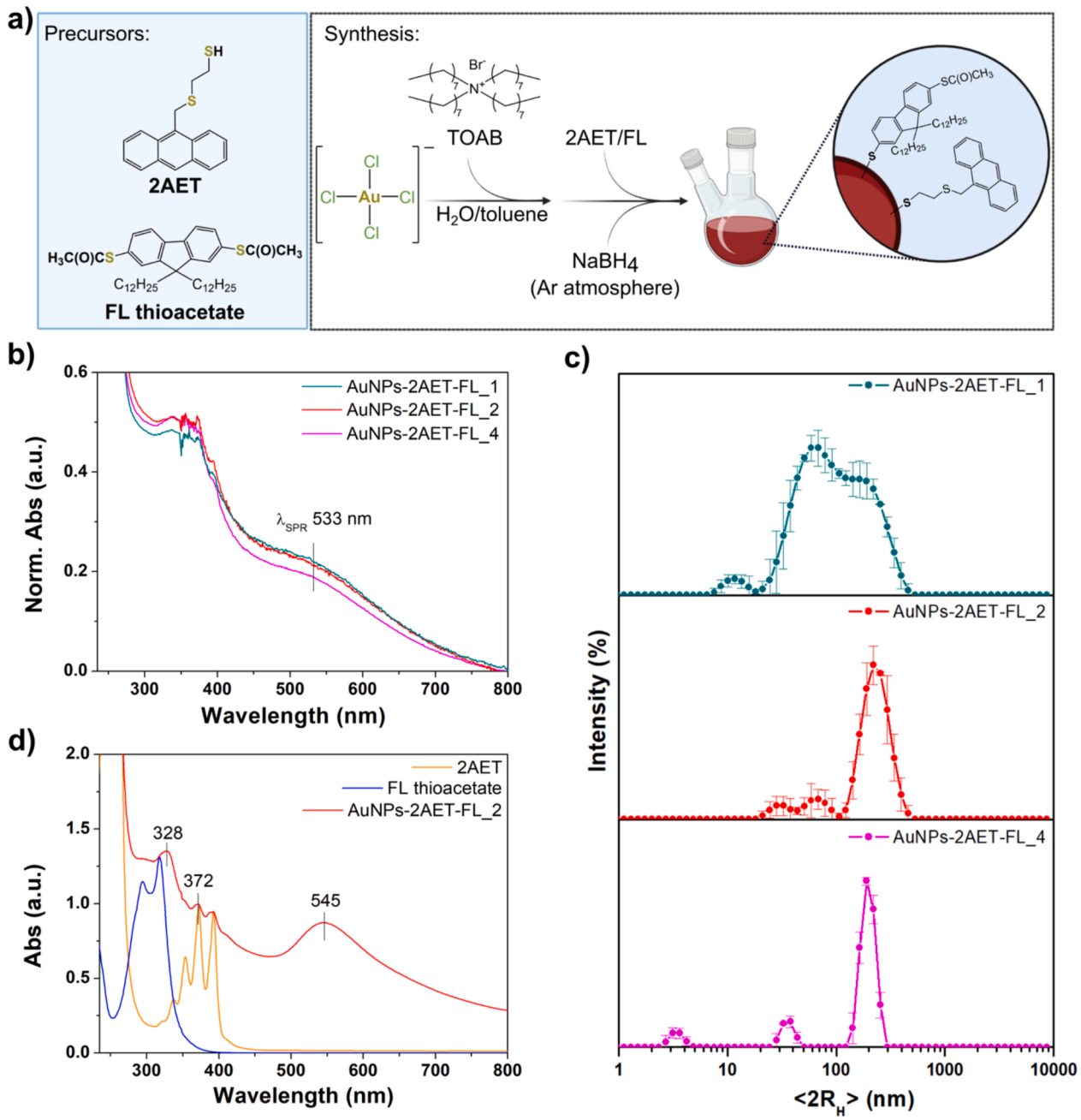

Fig. 1. Preparation and preliminary characterizations of AuNPs. a) Two-phase water/toluene synthesis scheme of AuNPs-2AET-FL adopted in this work. b) UV–Vis extinction spectra of freshly prepared colloidal AuNPs suspensions recorded in CH_2Cl_2. c) DLS particle size distribution in CH_2Cl_2 for freshly prepared AuNPs-2AET-FL_1 (dark cyan trace), AuNPs-2AET-FL_2 (red trace), AuNPs-2AET-FL_4 (magenta trace). d) UV–Vis extinction spectra of aged (1 year) AuNPs-2AET-FL_2 (red line), free 2AET (orange line) and FL thioacetate (blue line) ligands.

there was a small population centered at (12 ± 2) nm and the most intense population was found at (60 ± 25) nm, overlapping with that at (185 ± 65) nm. For AuNPs-2AET-FL_2 (Fig. 1c, red trace) two less intense populations were found at (30 ± 5) nm and at (68 ± 15) nm, whereas the most intense was centered at (260 ± 70) nm. In the AuNPs-2AET-FL_4 sample, a curve at (205 ± 30) nm appeared in the size distribution profile along with single populations at (37 ± 5) nm, and at (3 ± 1) nm (Fig. 1c, magenta trace). The use of a higher amount of FL ligand determine an increase in the polydispersity of the sample was found (for example comparing AuNPs-2AET-FL_1 with AuNPs-2AET-FL_4). It is worth mentioning that the FL ligand is used as bifunctional thioacetate derivative in the synthesis procedure, thus potentially leading to the formation of interconnected nanoparticles super-aggregates [33], contributing to the biggest population in the DLS profile, broadness of the SPR band and increased polydispersity [3,18].

Interestingly, after one year aging in CH_2Cl_2 suspension at room temperature and in a dark environment, UV–Vis analysis showed that the suspension of AuNPs-2AET-FL_2 (Fig. 1d) maintained its colloidal stability towards aggregation with a red-shift in the SPR band at 545 nm and a smaller FWHM value (66 nm) with respect to the freshly prepared sample in Fig. 1b. Absorption belonging to FL at 328 nm and 2AET at 372 nm also emerged from the UV–Vis profile. Conversely, AuNPs-2AET-FL_1 and AuNPs-2AET-FL_4 underwent irreversible aggregation, as demonstrated by the broadening of the SPR band in the aged samples (Fig. S3). The reported behavior can be ascribed to the partial time-induced release of the physisorbed thiol shell around gold core, which

contributes to colloidal gold nanoparticles stabilization [16]. According to the reported spectroscopic data, the profile, FWHM, and position of the plasmon band in three spectra (especially in the spectral region of 500–600 nm), freshly prepared AuNPs were similar in terms of shape (spherical NPs), composition (*Q* ratio between counterparts), and size distribution. This experimental procedure evidenced the ultimately reproducible synthesis protocol among molar ratio variations between reagents. However, long-term aging evidenced a different colloidal stability between samples, with the AuNPs-2AET-FL_2 showing the highest stability. This sample was selected for the preparation of the blends (see following paragraphs).

3.2. Photoluminescence properties of pristine gold nanoparticles

The emission properties of 2AET/FL-functionalized AuNPs were evaluated to give a better understanding of the impact of the synthesis protocol on the nanoparticle applications. The emission spectra of pristine 2AET dye and FL thioacetate were recorded using information-rich photoluminescence excitation-emission matrices (EEMs). In the case of 2AET in a dichloromethane solution, excitation was in the λ_{ex} = 335–395 nm wavelength range, with λ_{ex} = 375 nm being the wavelength of the maximum emission intensity for free dye (Fig. S1). The fluorophore showed an emission band with a maximum at 420 nm (Fig. 2a). On the other hand, EEM obtained for FL evidenced that excitation at 285 nm gave rise to the most intense emission spectrum (Fig. S2), with maximum corresponding emissions at 340 and 354 nm (Fig. 2b).

The measured emission spectra from aged functionalized AuNPs-2AET-FL_2 are reported in Fig. 2c, whereas spectra of AuNPs-2AET-FL_1 and AuNPs-2AET-FL_4 are reported in Fig. S4. For the excitation, two different wavelengths were explored: λ_{ex} = 333 nm (magenta line in Fig. 2c) and λ_{ex} = 370 nm (green line in Fig. 2c), the former capable of exciting the emission of both molecular components based on previous UV–Visible studies on aged samples (see paragraph 3.1). Excitation at 333 nm allowed to induce emission from both 2AET and FL, which overlapped in this spectral region with a significant contribution of the latter. Indeed, AuNPs-2AET-FL_2 sample excited at λ_{ex} = 333 nm showed an intense emission with λ_{em} = 362 nm, due to the presence of FL and 2AET ligands directly bonded to the gold surface, similar to that of AuNPs-2AET-FL_4 (Fig. S4). Compared with spectral features of 2AET and FL, a change in the spectral shape of functionalized AuNPs emission occurred, which goes beyond the trivial overlap of free ligands spectra. This result can be ascribed to the possible formation of Au–S bond, as reported for similar noble metal-interacted dyes [34]. In the case of AuNPs-2AET-FL_1 (Fig. S4), excitation at 333 nm did not produce considerable emission (same spectral shape around 360 nm, with much weaker intensity), which is in agreement with the lowest 2AET/FL (1:1) molar ratio. Selective emission from 2AET was evidenced at λ_{ex} = 370 nm, in which AuNPs-2AET-FL_2 showed a less intense emission with a maximum at λ_{em} = 416 nm, slightly blue-shifted compared with free 2AET dye.

Results showed that modulation it is possible to modulate gold colloids emission properties, taking advantage of the presence of mixed 2AET and FL on AuNPs according to different excitation wavelengths. In all cases, excitation in the proximity of surface plasmon resonance did not result in emission from gold cores or gold to thiols charge transfer phenomena (Fig. S4), confirming that spherical AuNPs with a diameter > 10 nm do not show intrinsic fluorescence [5,6].

3.3. Structural characterizations of pristine gold nanoparticles

Surface characterization of aged AuNPs was carried out by FTIR in the mid (4000–400 cm^{-1}) and far-infrared (600–200 cm^{-1}) regions. Spectra of AuNPs-2AET-FL_2 are reported in Fig. 3(a,b), whereas AuNPs-2AET-FL_1 and AuNPs-2AET-FL_4 spectra are reported in Fig. S5. Full assignments and comparison with pristine 2AET and FL thioacetate are reported in Table S1. The FTIR spectrum of AuNPs-2AET-FL_2 (Fig. 3a)

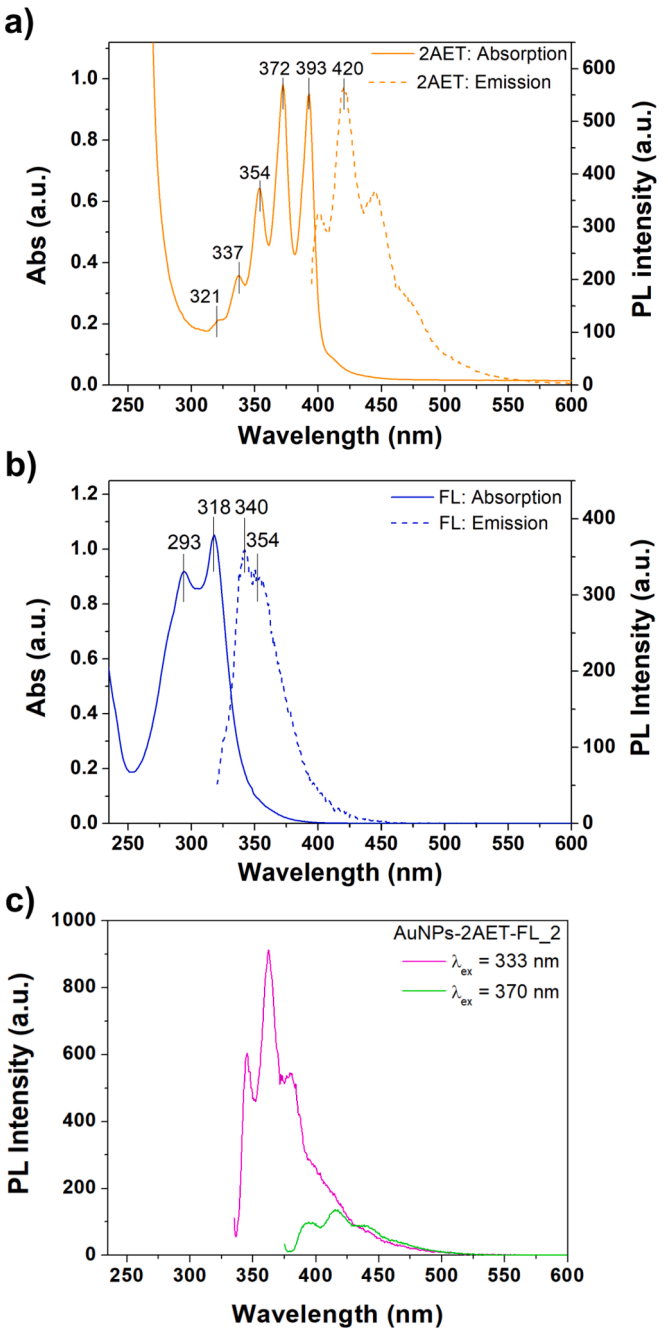

Fig. 2. Spectroscopic characterizations (UV–Vis, PL) of free 2AET and FL thiols and AuNPs-2AET-FL_2. a) Absorption (continuous line) and emission (dotted line) of 2AET dye in CH_2Cl_2 (λ_{ex} = 375 nm). b) Absorption (continuous line) and emission (dotted line) of FL thioacetate ligand in CH_2Cl_2 (λ_{ex} = 285 nm). c) Emission spectra of AuNPs recorded at two different excitation wavelengths: 333 nm (magenta line) and 370 nm (green line).

showed typical vibrations of aromatic portions of ligands: stretching (ν) of (═C—H) at 3061 cm^{-1} together with their *in-plane* bending δ(═C—H) at 1093, 1020 cm^{-1} and *out-of-plane* bending δ(═C—H) at 735 cm^{-1}, and those of ν(C—C) of the rings at 1663, 1594, 1482 cm^{-1}. Typical (C—C) deformations modes appeared at 880, 805 cm^{-1}. Aliphatic side chains of 2AET and FL gave rise to ν_{as}(—CH_3) at 2955 cm^{-1} (due to terminal carbons in —$C_{12}H_{25}$ chains of FL), whereas asymmetric ν_{as}(—CH_2) and symmetric ν_s(—CH_2) were found at 2926 and 2852 cm^{-1}, respectively. Less intense peaks ascribable to δ(—CH_3) at 1403 cm^{-1}, scissoring δ_s(—CH_2) at 1465 cm^{-1} and γ(—CH_2) at 1381 cm^{-1} were also found in the fingerprint region. Carbon-sulfur vibrations

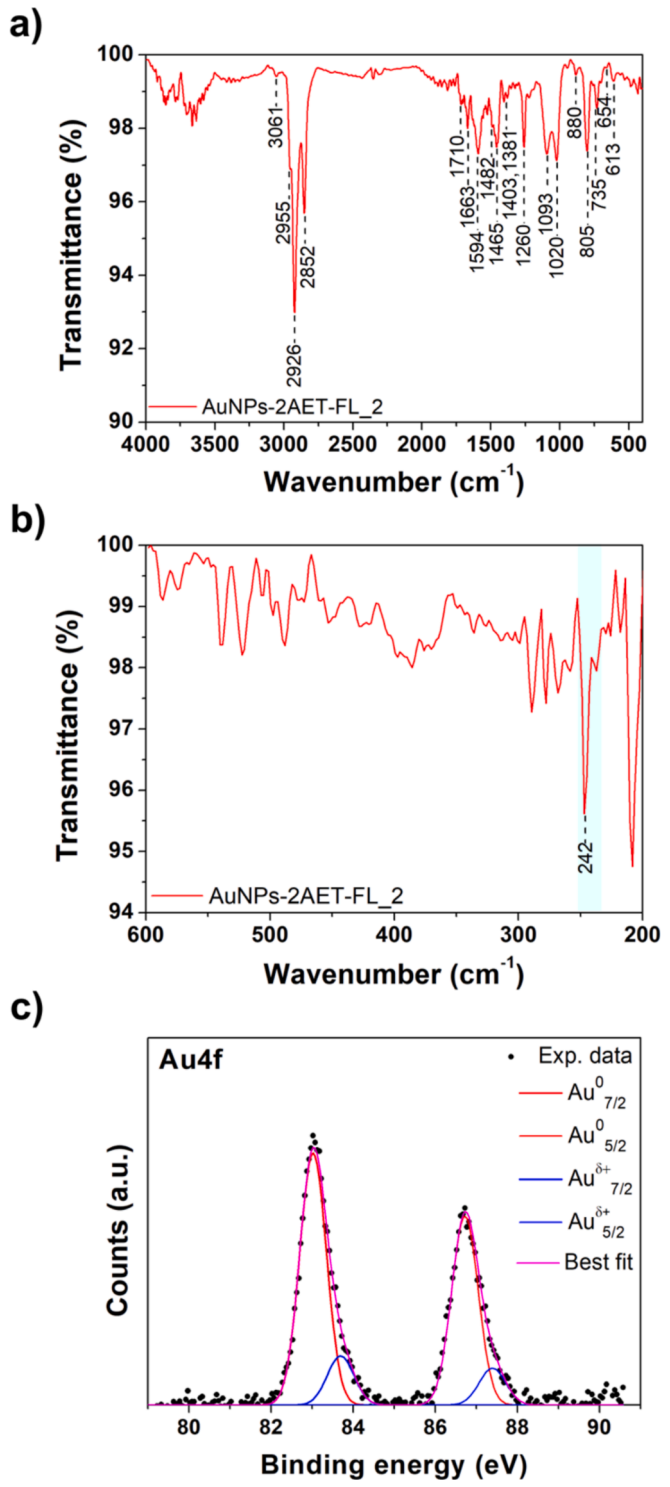

Fig. 3. Structural characterizations of AuNPs-2AET-FL_2. a) FT-IR in the 4000–400 cm^{-1} wavenumber range. b) Far-IR spectrum in the 600–200 cm^{-1} wavenumber range, Au–S stretching vibration at ca. 242 cm^{-1} is evidenced. c) Au4f core level spectrum. All analyses were conducted on dried solid thin film.

with different intensities at 654 and 613 cm^{-1} originate from aliphatic ν(C—S) of 2AET and aromatic ν(=C—S—C(O)CH_3) of FL, respectively. The weak signal at 1710 cm^{-1} was ascribed to ν(C=O), highlighting the presence of a small portion of unreacted thioacetate ending groups of FL. Notably, no signals corresponding to free ν(S—H) from 2AET ligand were found in the 2550–2600 cm^{-1} spectral region. To better evidence the successful functionalization, Far-IR spectra were recorded for AuNPs samples (Fig. 3b and Fig. S5). The region between 590–325 cm^{-1} was dominated by *in-plane* and *out-of-plane* ring deformation modes (523, 477, 326 cm^{-1}), whereas at ca. 300 cm^{-1} the band corresponding to —S—C—C deformation of 2AET aliphatic chain was found. Vibrations <300 cm^{-1} were mainly due to ρ(—CH_2), although in this region, the most important signal was detected at 242 cm^{-1}, attributed to the (Au—S) stretching vibration in AuNPs samples. This latter is normally found in the 280–170 cm^{-1} range, exhibiting two or three peaks depending on the sulfur binding modes [25].

SR-induced XPS measurements were carried out at the C1s, S2p and Au4f core levels. Full XPS data (BE, FWHM, atomic ratios) are reported in Table S2. C1s spectrum (Fig. S6) is made of three components. The first, fixed at 284.7 eV, is assigned to aromatic and C—S carbons; the second and the third at 286.8 and 288.9 eV to C—O and COOH carbons of contamination, respectively. S2p spectrum (Fig. S6) is made of five couples of spin–orbit doublets ($S2p_{3/2}$, $S2p_{1/2}$) of which the $S2p_{3/2}$ signal is taken as reference. $S2p_{3/2}$ signal at 161.4 eV is relative to thiols covalently bonded to gold nanoparticle surface. S2p3/2 signal at 163.0 eV is usually assigned to physisorbed thiols or disulfides. The last components at higher BE are due to oxidized sulfur atoms [35].

Au4f spectrum (Fig. 3c) shows two couples of spin–orbit ($Au4f_{7/2}$, $Au4f_{5/2}$) doublets, of which we consider as reference the $Au4f_{7/2}$ component. The $Au4f_{7/2}$ signal at 83.0 eV is due to metallic bulk Au(0) atoms of NPs, while those around 83.7 eV to surface Au atoms of nanoparticle involved in the covalent bond with sulfur atoms of functionalizing thiol ligands.

3.4. Morphological characterization of pristine gold nanoparticles

Morphological characterization of AuNPs was carried out by tapping mode AFM onto spin-coated samples from dichloromethane suspension. The corresponding AFM topography images of AuNPs-2AET-FL_2 dried on a glass substrate are shown in Fig. 4(a,b). As it can be seen, the observed nanostructures showed slightly elongated morphology with a maximum height in the 3–7 nm range, interconnected by an extended amorphous layer underneath.

More detailed morpho-structural imaging analyses have been provided using HR-TEM imaging. The HR-TEM images exhibit small nanoparticles with a darker contrast, chemically identified using EDX (Fig. 4c and Fig. S7). The EDX spectrum evidences the high purity of the aggregates, showing intense peaks belonging to Au species (Ni peaks are from the support grid). The small sulfur peak can be ascribed to the S atoms belonging to the thiol ligands. The morphometric imaging analysis of Fig. 4c identified quasi-spherical shape AuNPs, with a measured mean diameter of (4.1 ± 0.7) nm, having a polydispersity of about 17 %. It is noteworthy that the surface-to-surface distance of the nearest-neighbor nanoparticles has been estimated at about 1.30 nm, in agreement with to the organic FL bridge length. This result supports the formation of interconnected AuNPs networks. High-resolution image evidences the nanocrystal character of the typical AuNPs [36,37]. By measuring the crystalline lattices, the typical gold nanostructure of space group $Fm\bar{3}m$ with spacing $d_{(200)} = 0.206\ nm$ and $d_{(1\,1\,1)} = 0.239\ nm$ has been identified.

3.5. Synthesis and spectroscopic characterization of gold nanoparticles/PPA nanocomposite blends

Poly(phenylacetylene) (PPA) was used as a π-conjugated model polymer to obtain nanocomposite hybrid blends with AuNPs. Nanocomposite samples consisting of PPA and AuNPs-2AET-FL_2 were obtained at ambient temperature by mixing precalculated weight ratios of both PPA and AuNPs dopant in $CHCl_3$ according to Table 1 (experimental details are reported in paragraph 2.2.3).

Characteristic UV–Vis extinction spectra of nanocomposites, pristine fresh AuNPs and pure PPA are reported in Fig. 5**a**. Pure PPA showed a

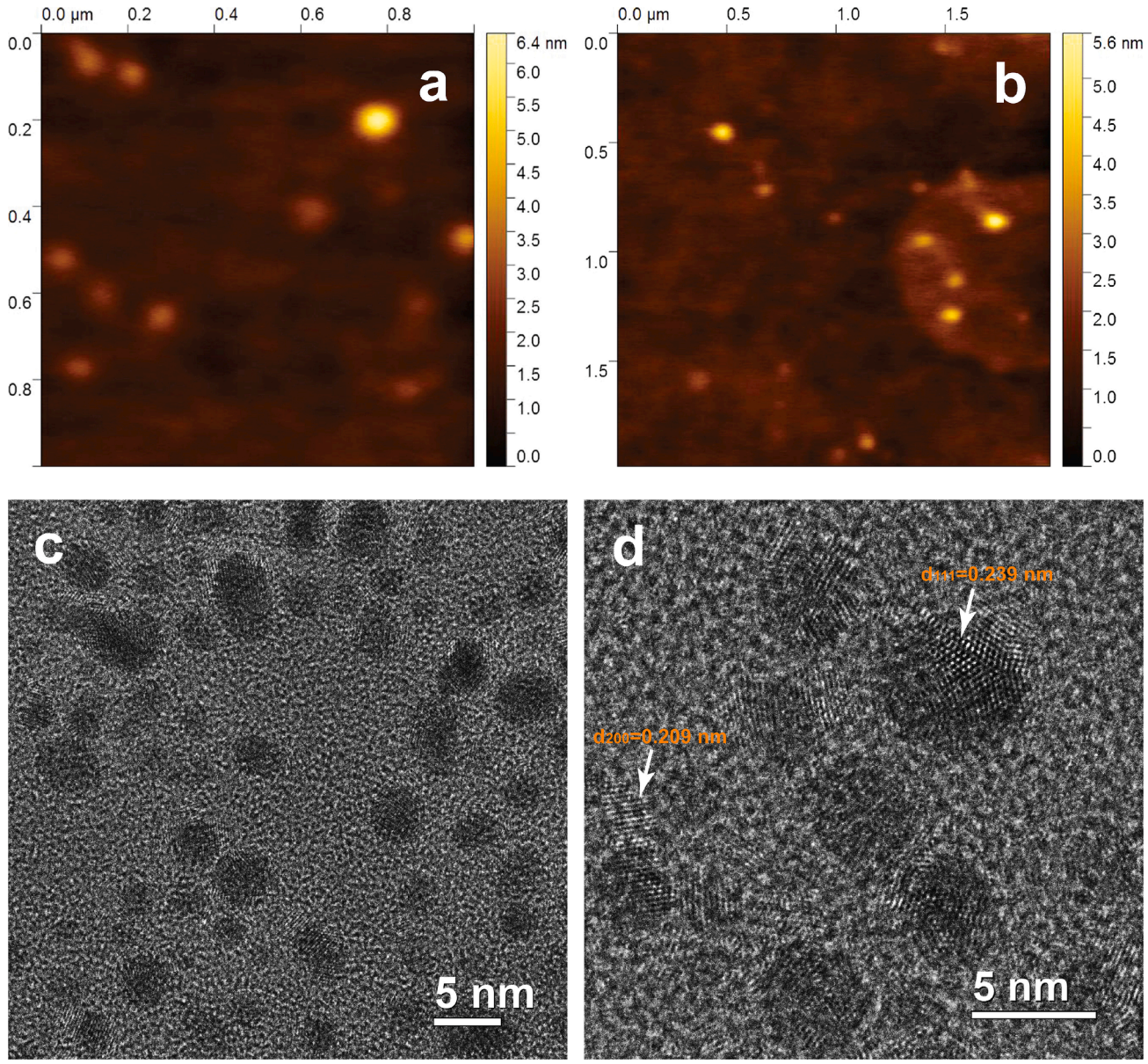

Fig. 4. Morpho-structural observations on AuNPs-2AET-FL_2. A-b) AFM measurements at different magnifications on AuNPs spin-coated onto Si/SiO_2 substrate from CH_2Cl_2 suspension and air dried. c) TEM image of crystalline AuNPs at medium magnification onto carbon amorphous film grid. D) HR-TEM micrograph of AuNPs with crystalline lattices spacing $d_{(200)} = 0.206$ nm and $d_{(1\,1\,1)} = 0.239$ nm.

Table 1
Conditions used for the nanocomposites sample preparation.

Sample	AuNPs-2AET-FL_2 (%wt.)	PPA (%wt.)
B10	10	90
B30	30	70
B50	50	50
B70	70	30
B90	90	10

predominant *cis*-transoid conformation with intense absorptions centered at 250 nm due to the π–π* transitions of the phenyl groups and broad, less intense shoulder bands at 330 nm and 394 nm due to the π–π* transition of conjugated main chain between HOMO and LUMO along their axis direction [38,39]. Nanocomposite samples can be distinguished by the appearance of the typical SPR band of AuNPs at 533 nm, which becomes more evident in the B90 sample (Fig. 5b), whereas for B10 and B30 the absorption is still clearly dominated by the polymer. The SPR band of AuNPs did not show reasonable changes compared to pristine AuNPs, both in terms of position and width, thus demonstrating that blending with PPA did not induce nanoparticle aggregation. The stability towards aggregation can be ascribed to a chemical matching between surface functionalizing agents on NPs surface bearing aryl moieties and the phenyl rings of the polymer matrix [40]. All spectra were characterized by the main absorption edge at ca. 250 nm mainly consistent with the presence of PPA and a red shift up to 260 nm by increasing the AuNPs amount (sample B90). Moreover, in B70 and B90, this band appears to be distorted. Notably, a change also occurs in the absorptions in the 300–450 nm wavelength range (those associated with π–π* transitions of the polymer chain double bonds). In this region, B10 and B30 profiles linearly follow that of the polymer, whereas changes in the absorption intensities were found for B50, B70, B90 samples. The reported shifts and distortions in the UV–vis bands could be ascribed to (i) a change in the crystalline phase in the nanocomposites and thus, in the optical energy gap (E_g) [41], and (ii) the formation of interfacial

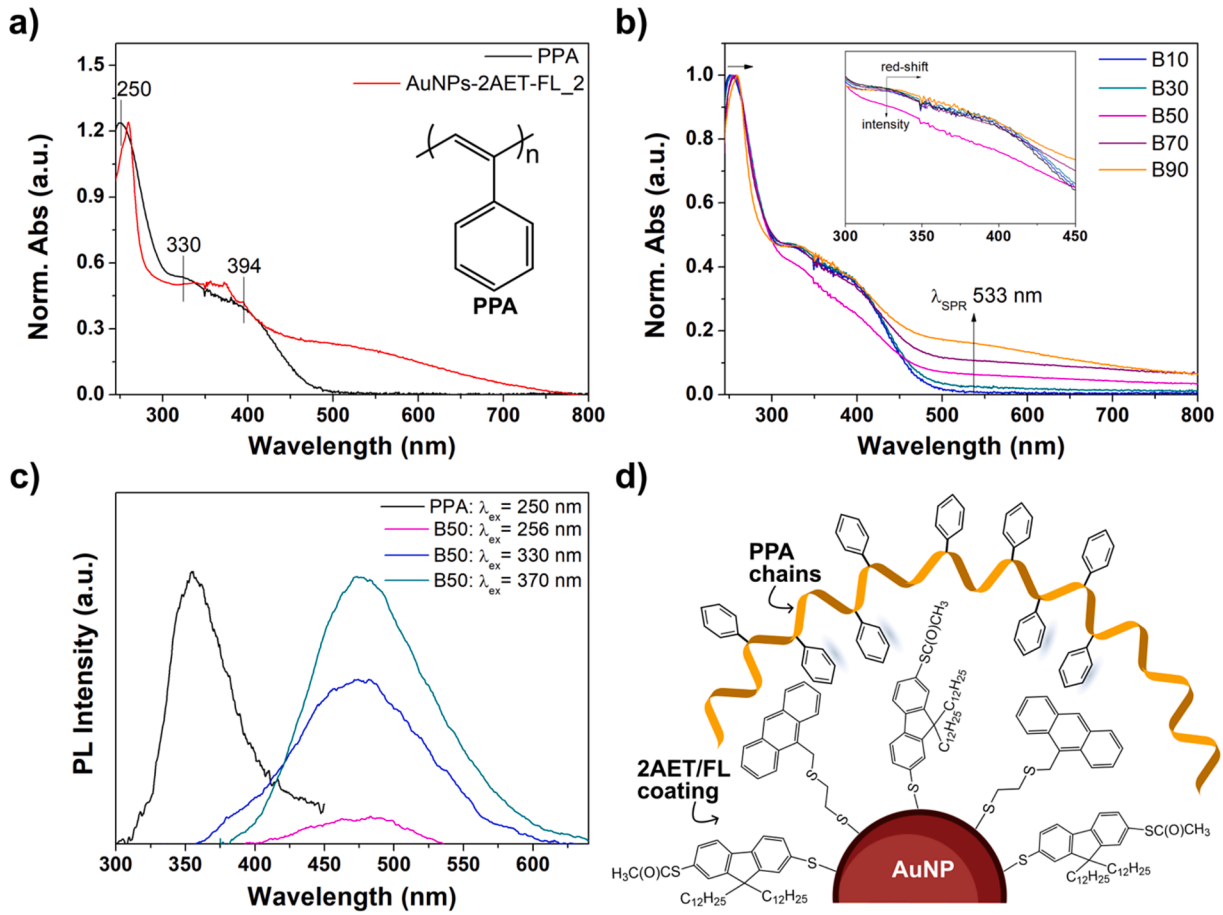

Fig. 5. Spectroscopic characterizations (UV–Vis, PL) of pure PPA and related AuNPs blends. a) UV–visible extinction spectra of pure PPA ($CHCl_3$) and pristine AuNPs-2AET-FL_2 (CH_2Cl_2). Inset: chemical structure of PPA. b) UV–visible spectra of AuNPs-2AET-FL_2/PPA nanocomposite blends containing different amounts of AuNPs. c) Emission spectra in CH_2Cl_2 of PPA (black line) and B50 at different excitation wavelengths. For labels refer to Table 1. d) Possible interaction mechanism occurring between AuNPs-2AET-FL_2 and PPA in the nanocomposites.

non-covalent π–π stacking between PPA chains and aromatic thiols on AuNPs, as previously reported in AuNPs/P3HT polymer blends [18], highlighting the complexity of AuNPs/polymer interactions. In particular, the hypsochromic shift and intensity decrease in the visible band of PPA (300–500 nm) is the result of a decrease in the main-chain conjugation [42,43]. The shortening of the extent delocalization of π-electrons can be ascribed to charge-transfer phenomena across the metal/organic interfaces probably interacting through weak π–π stacking which proved to facilitate the electron transfer process [44,45].

Selected photoluminescence spectra of pure PPA and B50 nanocomposites are given in Fig. 5c. Pristine polymer showed an emission maximum at 356 nm at $\lambda_{ex} = 250$ nm, whereas at $\lambda_{ex} = 330$ nm and $\lambda_{ex} = 394$ nm PPA resulted in a less intense emission at 384 and 471 nm, respectively (Fig. S8). In the AuNPs/PPA B50 blend, excitation at 256 nm gave only a small contribution (Fig. S8), arising from the polymeric counterpart. Conversely, $\lambda_{ex} = 330$ nm resulted in an emission spectrum with a maximum at 475 nm and a shoulder band at 390 nm (whose profile linearly follows that at $\lambda_{ex} = 325$ nm, see Fig. S8). The shoulder band in the nanocomposite originates from PPA and disappeared for $\lambda_{ex} = 330$ nm with an increase in the emission intensity at 475 nm. The latter can be ascribed to the 2AET dye functionalizing AuNPs, with a red shift of 56 nm compared with the emission of pristine functionalized AuNPs (see paragraph 3.2). The redshift can be due to the formation of exciplex (hole-transporting molecules which provide electrons and electron-transporting materials able to accept electrons) in the blended system originating from interchain interactions [46,47]. In this specific case, this behavior is reflected in the suppression of radiative decay in favor of charge transfer phenomena likely due to polymer addition. The possible interaction is schematized in Fig. 5d.

The morphology of PPA and nanocomposite blends spin-coated as thin films on a solid substrate was investigated by AFM. Nanometric imaging of PPA in the absence of AuNPs at two different magnifications is shown in Fig. 6a. Neat polymer showed an irregular flat morphology (with cavities induced by solvent evaporation), forming a layer of (4 ± 1) nm average thickness, partially wrapped at the edge of the cavities. AFM topography of NPs/PPA blend image is displayed in Fig. 6b. Qualitatively, at the AuNPs concentrations herein used, the general structure of PPA was not altered by the addition of NPs, the thickness of the blend being almost unaltered and estimated to be (4.6 ± 0.8) nm (Fig. S9). However, in this case, several nanostructures were found entrapped inside the polymer matrix since the alone NPs of 4.1 nm were estimated by HR-TEM. The images clearly show the presence of round-shaped protrusions uniformly distributed within the polymer, which cause a remarkable variation in the maximum sample dimension in z direction.

3.6. *Electrical properties*

Band gap energy (E_g) of pristine functionalized AuNPs, PPA and related blends was estimated using the Tauc plot method, further developed by Davis and Mott from UV–Vis extinction spectra [48]. First, the energy-dependent absorption coefficient α was calculated by the Lambert–Beer's modulus following Eq. (2):

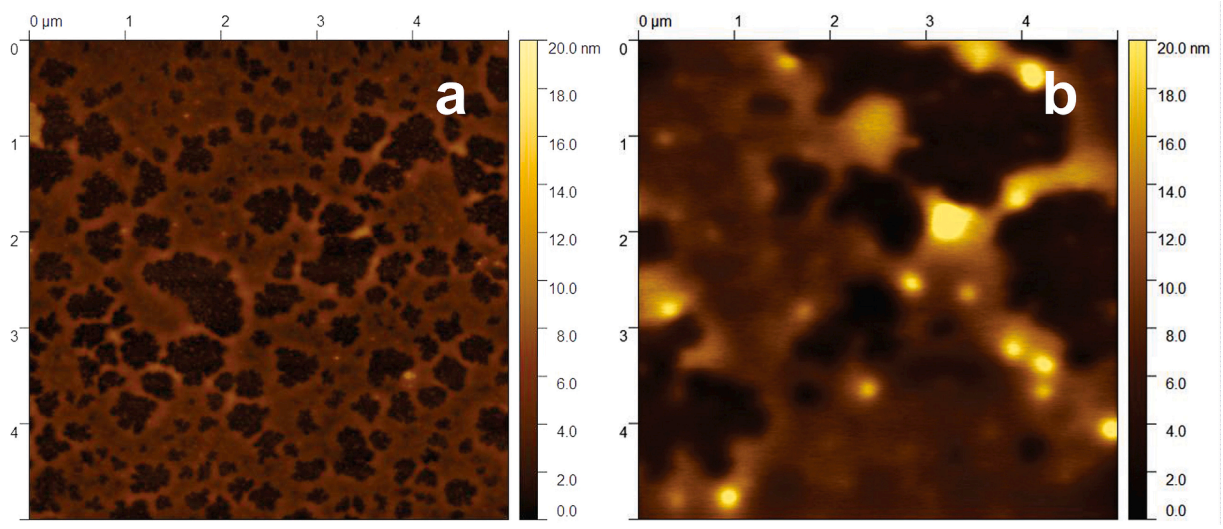

Fig. 6. AFM topography images of a) pure PPA and b) AuNPs-2AET-FL_2/PPA 50:50 %wt. nanocomposite blend. Samples were spin-coated onto Si/SiO_2 substrate from their organic suspensions and air dried.

$$\alpha(\nu) = 2.303 \cdot \left(\frac{A}{d}\right) \tag{2}$$

where α is estimated by absorbance (A) and thickness of the optical path length (d, in cm). The absorption coefficient α dependent on the incident photon energy can be expressed by the typical Eq. (3):

$$(\alpha h\nu) = \beta(h\nu - E_g)^{\gamma} \text{for} \, h\nu > E_g \tag{3}$$

where β is the absorption constant (associated with the separation of electrical conductivity and energy level), h is the Planck's constant (J·s), ν is the photon's frequency (s^{-1}), and the γ exponent factor is related to the nature of possible electronic transition: $\gamma = 2$ (indirect transition) allowed and $\gamma = 1/2$ (direct transition), respectively [40,49].

Spectra obtained by plotting $(\alpha h\nu)^2$ and $(\alpha h\nu)^{1/2}$ as a function of energy (hν) are reported in Fig. S10, and results summarized in Table 2. Herein, only the optical transition band gaps (involved in the excitation of electrons from the valance band to conduction band using photons of selected frequency) will be considered. It is worth noting that the optical band gap herein considered is important for applications such as solar cells, whereas the electronic band gap (removal or injection of electrons from the semiconductor valence band), usually higher than the optical band gap, should be considered for devices such as light emitting diodes and laser diodes. However, for amorphous materials it is hard to estimate whether the band is direct or indirect [50].

Gold nanoparticles showed optical E_g values of about 4.0 eV, consistent with an insulating behavior (>4 eV), whereas a lower E_g of ca. 2 eV value was found for typical semiconductor PPA [51,52]. For AuNPs/PPA nanocomposites, gold nanoparticles incorporation causes a variation in the E_g values. Optical band gap values decrease from 2.47 to 2.15 eV for direct transitions, whereas they decrease from 2.75 to 2.68 eV for indirect transitions (with respect to pure PPA) with increasing the concentration of gold nanoparticles (Table 2). Thus, the band gap value can be tuned according to AuNPs filling, achieving a reduction (13 % for direct transitions, 3 % for indirect transitions) when compared to the values for AuNPs functionalized with 1-dodecanthiol in P3HT:PCBM film [53], and similar values to those of oleylamine-functionalized Au- and AgNPs/P3HT:PCBM blends [54], and AuNP-doped P3HT [55]. These results can be clarified in terms of (1) increase in the disorder caused by the polymer structural alteration, *e.g.*, deformities caused by localized states within the energy bandgap after AuNPs addition, and (2) creation of charge transfer complexes between functionalized gold nanoparticles and PPA structures [40,56].

Table 2
Direct and indirect optical band gap values obtained for AuNPs-2AET-FL_2, pure PPA, and AuNPs/PPA nanocomposite blends.

Sample	Optical Band gap (eV) ± 0.05 eV	
	Direct	Indirect
AuNPs-2AET-FL_2	4.13	4.50
PPA	2.47	2.75
B10	2.44	2.73
B30	2.41	2.72
B50	2.35	2.76
B70	2.34	2.69
B90	2.15	2.68

Electrical conductivity at room temperature (σ) for AuNPs-2AET-FL_2, PPA, and nanocomposites was calculated using Eq. (4) and Eq. (5) [57]:

$$\sigma = \frac{G \cdot L}{t \cdot W} \tag{4}$$

$$Norm.relativeconductivity(\%) = \frac{(\sigma - \sigma_{AuNPs})}{\sigma_{AuNPs}} \cdot 100 \tag{5}$$

where G is the conductance (1/R in 1/Ω = S) derived from the slope of I/V measurements, t is the thickness of each film (in m) measured by AFM of (4.6 ± 0.8) nm (see paragraph 3.5), L is the length between electrodes (in m) and W is the electrode length (in m) both depending on electrode design. In this case, electrical conductivity was in the range of (9.3 ± 0.9)·10^{-8} S m^{-1} (pure PPA) to (23 ± 2)·10^{-8} S m^{-1} in polymer blends (Table S3). Herein, a similar film thickness was assumed for all formulations, since it is mainly governed by spin coating conditions (rotational speed, suspension concentration, rate of solvent evaporation) [58]. Normalized relative conductivity percentages reported in Fig. 7 clearly showed a conductivity increase as the AuNPs content increased. In particular, B50, B70, B90 significantly deviate with respect to other samples with (23 ± 2)%, (86 ± 9)%, and (144 ± 14)% conductivity gain to that of pristine functionalized AuNPs (considered as 100 %), respectively. In particular, a significant enhancement in the conductivity was found with respect to pure PPA, which acts as a doping material for AuNPs in B70 and B90 nanocomposites. It is worth mentioning that processing methods, secondary doping and post-treatments have been verified to affect electrical conductivity values [59] and they are strongly dependent on the molecular arrangement of the polymer chains in the film (*e.g.*, edge-on, face-on configurations) that leads to different

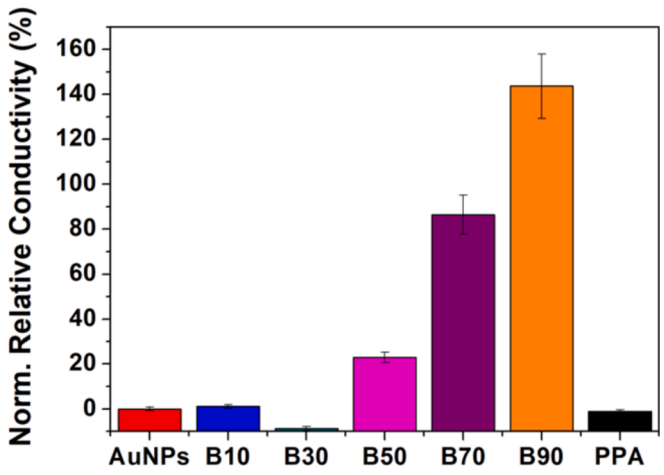

Fig. 7. Relative electrical conductivity (%) calculated for pristine AuNPs-2AET-FL_2, pure PPA and related nanocomposite blends. All values are normalized according to AuNPs electrical conductivity (σ).

interface resistances [60]. Concerning practical applications, relative current ($\Delta I/I_0$ %) [61] was plotted for different samples at 5 V and 10 V (Fig. S11). For both, a similar trend was found with a 60 % current improvement after 90 % wt. of AuNPs addition. As reported for similar AuNPs/polymer nanocomposites, the enhancement of the electrical properties after blending procedure may be attributed to an increase in the amorphous phase of the polymeric matrix (due to the inclusion of AuNPs), which lowers the energy barrier and permits ion transport [18,62].

4. Conclusions

A typical two-phase wet chemical reduction method produced gold nanoparticles functionalized with two different thiols: a bifunctional synthetic 9,9-didodecyl-2,7-bis(acetylthio)fluorene (FL thioacetate) and a synthetic organic fluorescent dye 2-(anthracene-9-ylthio)ethane-1-thiol (2AET) to obtain AuNPs-2AET-FL colloids. Different molar ratios among precursors were explored, finding that freshly prepared samples were quite similar, showing an SPR band at 533 nm, as evidenced by UV–Vis measurements. At higher FL content during synthesis, smaller gold nanoparticles were obtained (with hydrodynamic diameter $<2R_H>$ of about 3 nm), together with an increase in the polydispersity of the sample. After one year of aging, the AuNPs-2AET-FL_2 (2AET/FL 1:2 M ratio) remained stable in its dichloromethane suspension, with a sharp surface plasmon band at 545 nm and typical absorptions arising from surface functionalizing thiols. Solid-state morphological analysis (TEM, AFM) conducted on the latter evidenced AuNPs of quasi-spherical shape with a measured diameter of (4.1 ± 0.7) nm on average, with a polydispersity of about 17 %. Surface characterization (FTIR, Far-IR, SR-XPS) confirmed the occurred functionalization. Photoluminescence measurements evidenced that it is possible to modulate the AuNPs emission: excitation at 333 nm induced emission from both 2AET and FL, whereas 2AET selective emission was found with λ_{ex} = 370 nm, whereas no fluorescence arose from the gold core (λ_{ex} = 533 and 545 nm). New nanocomposites were synthesized using a simple blending approach based on a poly(phenylacetylene) (PPA) matrix doped with the produced AuNPs. Blends varying AuNPs-2AET-FL/poly (phenylacetylene) (PPA) composition were obtained: 10/90, 30/70, 50/50, 70/30, 90/10 %. After blending, a blue-shift in the UV–Vis spectra (300–500 nm spectral region) of the B50 and B90 samples was ascribed to a reduction of the extent of delocalization of π-electrons and the appearance of charge-transfer phenomena across the metal/organic interfaces, possibly interacting through π–π stacking. Charge-transfer reduced the radiative decay of the PPA matrix in emission spectra, with a consequent red shift in the emission maxima of functionalizing agents on AuNPs compared with pristine nanoparticles. Electrical characterization revealed a reduction in the band gap up to 2.15 eV for direct transitions and up to 2.68 eV for indirect transitions after addition of 90 %wt of AuNPs in the PPA matrix. Nanocomposites deposited as thin films (thickness of 4.6 ± 0.8 nm) showed a progressive increase in the electrical conductivity with respect to pristine, functionalized AuNPs reaching 144 % gain in the case of B90 with respect to pristine, functionalized AuNPs. In particular, an increase of about 2.5 times the relative conductivity value of pure PPA was obtained at 90 % AuNPs loading.

CRediT authorship contribution statement

Sara Cerra: Investigation, Writing – original draft. **Damiano Cirri:** Investigation, Visualization. **Chiara Gabbiani:** Investigation, Visualization. **Alessandro Pratesi:** Investigation, Visualization. **Souren Grigorian:** Investigation, Visualization. **Roberto Matassa:** Investigation, Visualization. **Juan G. Lozano:** Investigation, Visualization. **Ana M. Beltrán:** Investigation, Visualization. **Angela Capocefalo:** Investigation, Visualization. **Claudia Fasolato:** Investigation, Visualization. **Francesca A. Scaramuzzo:** Investigation, Visualization. **Martina Marsotto:** Investigation, Visualization. **Chiara Battocchio:** Investigation, Visualization. **Tommaso A. Salamone:** Investigation, Visualization. **Beatrice Pennacchi:** Investigation, Visualization. **Martina Mercurio:** Investigation, Visualization. **Ilaria Fratoddi:** Conceptualization, Supervision, Writing – review & editing.

Declaration of competing interest

The authors declare that they have no known competing financial interests or personal relationships that could have appeared to influence the work reported in this paper.

Acknowledgements

The authors gratefully acknowledge for the financial support Sapienza funding Grant Ateneo Ricerca 2022 (RM1221867C322C1). The authors acknowledge financial support from the National Quantum Science Technology Institute within PNRR MUR project PE0000023-NQSTI. The authors are grateful to the Centro de Investigación, Tecnología e Innovación (CITIUS) de la Universidad de Sevilla, Spain, for the provision of their facilities and expertise. Authors from Roma Tre University gratefully acknowledge the CERIC-ERIC Consortium for the access to experimental facilities (MSB at Elettra) and financial support. S. G. is grateful for the ATHENA European University project 2021–2022, in cooperation with University of Orléans and Comenius International Fellowship, University of Siegen, 2024. DC and CG acknowledge the support of the European Union by the Next Generation EU project ECS00000017 'Ecosistema dell'Innovazione' Tuscany Health Ecosystem (THE, PNRR, Spoke 4: Nanotechnologies for diagnosis and therapy).The Centre for Instrumentation Sharing (CISUP), University of Pisa, is also acknowledged for ESI-MS analysis.

Appendix A. Supplementary data

Figure S1: Characterizations of 2AET dye. Figure S2: Characterizations of FL thioacetate ligand. Figure S3: UV–Visible spectra of AuNPs after one year aging. Figure S4: Photoluminescence of AuNPs. Figure S5: FTIR of AuNPs. Figure S6: SR-XPS of AuNPs. Figure S7: Morphochemical characterizations. Figure S8: Photoluminescence of PPA and B50. Figure S9: AFM thickness profile. Figure S10: Tauc plot. Figure S11: Relative current trend. Table S1: FTIR bands in the mid-infrared region and their assignment. Table S2: SR-XPS data. Table S3: Electrical conductivity values. Supplementary data to this article can be found online at https://doi.org/10.1016/j.ica.2025.122553.

Data availability

Data will be made available on request.

References

[1] L. Wang, M. Hasanzadeh Kafshgari, M. Meunier, Optical properties and applications of plasmonic-metal nanoparticles, *Adv. Funct. Mater.* 30 (2020) 2005400, https://doi.org/10.1002/adfm.202005400.

[2] Y. Fu, Z. Yin, L. Qin, D. Huang, H. Yi, X. Liu, S. Liu, M. Zhang, B. Li, L. Li, W. Wang, X. Zhou, Y. Li, G. Zeng, C. Lai, Recent progress of noble metals with tailored features in catalytic oxidation for organic pollutants degradation, *J. Hazard. Mat.* 422 (2022) 126950, https://doi.org/10.1016/j.jhazmat.2021.126950.

[3] S. Cerra, T.A. Salamone, A. Bearzotti, F. Hajareh Haghighi, M. Mercurio, M. Marsotto, C. Battocchio, R. Fioravanti, M. Diociaiuti, I. Fratoddi, Thiol-functionalized palladium nanoparticles networks: synthesis, characterization, and room temperature (toxic) vapor detection, *Part. Part. Syst. Charact.* 40 (2023) 2200189, https://doi.org/10.1002/ppsc.202200189.

[4] Z. Guo, G. Yu, Z. Zhang, Y. Han, G. Guan, W. Yang, M. Han, Intrinsic optical properties and emerging applications of gold nanostructures, *Adv. Mater.* 35 (2023) 2206700, https://doi.org/10.1002/adma.202206700.

[5] P. Anger, P. Bharadwaj, L. Novotny, Enhancement and quenching of single-molecule fluorescence, Phys. Rev. Lett. 96 (2006) 113002, https://doi.org/10.1103/PhysRevLett.96.113002.

[6] G. Schneider, G. Decher, N. Nerambourg, R. Praho, M.H.V. Werts, M. Blanchard-Desce, Distance-dependent fluorescence quenching on gold nanoparticles ensheathed with layer-by-layer assembled polyelectrolytes, *Nano Lett.* 6 (2006) 530–536, https://doi.org/10.1021/nl052441s.

[7] O. Karakurt, E. Alemdar, M.C. Erer, D. Cevher, S. Gulmez, U. Taylan, S.C. Cevher, G. Hizalan Ozsoy, B. Ortac, A. Cirpan, Boosting the efficiency of organic solar cells via plasmonic gold nanoparticles and thiol functionalized conjugated polymer, *Dyes Pigm.* 208 (2023) 110818, https://doi.org/10.1016/j.dyepig.2022.110818.

[8] N. Zhou, V. López-Puente, Q. Wang, L. Polavarapu, I. Pastoriza-Santos, Q.-H. Xu, Plasmon-enhanced light harvesting: applications in enhanced photocatalysis, photodynamic therapy and photovoltaics, *RSC Adv.* 5 (2015) 29076–29097, https://doi.org/10.1039/C5RA01819F.

[9] G. Barbillon, Plasmonics and its applications, *Materials* 12 (2019) 1502, https://doi.org/10.3390/ma12091502.

[10] J.V. Pellegrotti, G.P. Acuna, A. Puchkova, P. Holzmeister, A. Gietl, B. Lalkens, F. D. Stefani, P. Tinnefeld, Controlled reduction of photobleaching in DNA origami–gold nanoparticle hybrids, *Nano Lett.* 14 (2014) 2831–2836, https://doi.org/10.1021/nl500841n.

[11] N. Ibrayev, E. Seliverstova, G. Omarova, A. Kanapina, A. Ishchenko, Plasmon Au nanoparticles effect on the spectral and fluorescent properties of indopolycarbocyanine dyes, *Mater. Today Proc.* 71 (2022) 100–104, https://doi.org/10.1016/j.matpr.2022.09.615.

[12] B.R. Kumar, N.S. Basheer, A. Kurian, S.D. George, Study of concentration-dependent quantum yield of Rhodamine 6G by gold nanoparticles using thermal-lens technique, *Appl. Phys. B* 115 (2014) 335–342, https://doi.org/10.1007/s00340-013-5608-x.

[13] J. John, L. Thomas, A. Kurian, S.D. George, Modulating fluorescence quantum yield of highly concentrated fluorescein using differently shaped green synthesized gold nanoparticles, *J. Lumin.* 172 (2016) 39–46, https://doi.org/10.1016/j.jlumin.2015.11.005.

[14] A. Fratoddi, I. Cartoni, D. Venditti, P. Catone, A. O'Keeffe, F. Paladini, S. Toschi, F. Turchini, G. Sciubba, C. Testa, L. Battocchio, R.P. Carlini, E. Zaccaria, I. Magnano, L.A. Pis, Gold nanoparticles functionalized by rhodamine B isothiocyanate: a new tool to control plasmonic effects, *J. Colloid Interface Sci.* 513 (2018) 10–19, https://doi.org/10.1016/j.jcis.2017.11.010.

[15] H. Häkkinen, The gold–sulfur interface at the nanoscale, *Nature Chem.* 4 (2012) 443–455, https://doi.org/10.1038/nchem.1352.

[16] I. Fratoddi, S. Cerra, T.A. Salamone, R. Fioravanti, F. Sciubba, E. Zampetti, A. Macagnano, A. Generosi, B. Paci, F.A. Scaramuzzo, R. Matassa, G. Familiari, C. Battocchio, M. Marsotto, P. Papa, A. Bearzotti, Functionalized gold nanoparticles as an active layer for mercury vapor detection at room temperature, *ACS Appl. Nano Mater.* 4 (2021) 2930–2940, https://doi.org/10.1021/acsanm.1c00074.

[17] G.A. Kelesidis, D. Gao, F.H.L. Starsich, S.E. Pratsinis, Light extinction by agglomerates of gold nanoparticles: a plasmon ruler for sub-10 nm interparticle distances, *Anal. Chem.* 94 (2022) 5310–5316, https://doi.org/10.1021/acs.analchem.1c05145.

[18] S. Grigorian, L. Fontana, S. Cerra, U. Pietsch, F.A. Scaramuzzo, I. Fratoddi, Superior transport behavior of gold nanoparticles/P3HT blends by tuning optical and structural properties, *Synth. Met.* 283 (2022) 116973, https://doi.org/10.1016/j.synthmet.2021.116973.

[19] M. Muhammed Shameem, S.M. Sasikanth, R. Annamalai, R. Ganapathi Raman, A brief review on polymer nanocomposites and its applications, *Mater. Today Proc.* 45 (2021) 2536–2539, https://doi.org/10.1016/j.matpr.2020.11.254.

[20] M. Núñez-Martínez, S. Arias, J. Bergueiro, E. Quiñoá, R. Riguera, F. Freire, The role of polymer–AuNP interaction in the stimuli-response properties of PPA–AuNP nanocomposites, *Macromol. Rapid Commun.* 43 (2022) 2100616, https://doi.org/10.1002/marc.202100616.

[21] C. Cametti, P. Codastefano, R. D'Amato, A. Furlani, M.V. Russo, Static and dynamic light scattering measurements of polyphenylacetylene (PPA) in different organic solvents (tetrahydrofuran, toluene and chloroform), *Synth. Met.* 114 (2000) 173–179, https://doi.org/10.1016/S0379-6779(00)00245-9.

[22] M. Avram, G.H. Mateescu, Infrared Spectroscopy: Applications in Organic Chemistry, 2nd ed., R. E. Krieger Publishing Company, Huntington, New York, 1978.

[23] R.W. Silverstein, F.X. Webster, D.J. Kiemle, Chapter 2: Infrared spectrometry. *Spectrometric Identification of Organic Compounds*, 7th ed., John Wiley & Sons Inc, Hoboken, New Jersey, 2005.

[24] Y. Chen, H. Liu, Y. Deng, D.B. Veksler, M.S. Shur, X.-C. Zhang, D. Schauki, M.J. Fitch, R. Osiander, C. Dodson, J.B. Spicer, Spectroscopic characterization of explosives in the far-infrared region, in: R.J. Hwu, D.L. Woolard (Eds.), Orlando, FL, 2004: p. 1. https://doi.org/10.1117/12.540945.

[25] J. Petroski, M. Chou, C. Creutz, The coordination chemistry of gold surfaces: Formation and far-infrared spectra of alkanethiolate-capped gold nanoparticles, *J. Organomet. Chem.* 694 (2009) 1138–1143, https://doi.org/10.1016/j.jorganchem.2008.11.057.

[26] D. Lin-Vien, The Handbook of Infrared and Raman Characteristic Frequencies of Organic Molecules, Academic Press, Boston, 1991.

[27] N.O. Devarie Baez, J.A. Reisz, C.M. Furdui, Mass spectrometry in studies of protein thiol chemistry and signaling: opportunities and caveats, *Free Radic. Biol. Med.* 80 (2015) 191–211, https://doi.org/10.1016/j.freeradbiomed.2014.09.016.

[28] M. Brust, M. Walker, D. Bethell, D.J. Schiffrin, R. Whyman, Synthesis of thiol-derivatized gold nanoparticles in a 1994, 2-phase liquid-liquid system, *J. Chem. Soc. Chem. Commun.* (1994) 801–802, https://doi.org/10.1039/C39940000801.

[29] C.C. Lim, Far-infrared high-density polyethylene windows for low-temperature and moderate-pressure applications, Rev. Sci. Instrum. 57 (1986) 1419–1421, https://doi.org/10.1063/1.1138613.

[30] D.E. Mustafa, T. Yang, Z. Xuan, S. Chen, H. Tu, A. Zhang, Surface plasmon coupling effect of gold nanoparticles with different shape and size on conventional surface plasmon resonance signal, *Plasmonics* 5 (2010) 221–231, https://doi.org/10.1007/s11468-010-9141-z.

[31] S.K. Ghosh, T. Pal, Interparticle coupling effect on the surface plasmon resonance of gold nanoparticles: from theory to applications, *Chem. Rev.* 107 (2007) 4797–4862, https://doi.org/10.1021/cr0680282.

[32] A. Bearzotti, P. Papa, A. Macagnano, E. Zampetti, I. Venditti, R. Fioravanti, L. Fontana, R. Matassa, G. Familiari, I. Fratoddi, Environmental Hg vapours adsorption and detection by using functionalized gold nanoparticles network, *J. Environ. Chem. Eng.* 6 (2018) 4706–4713, https://doi.org/10.1016/j.jece.2018.07.013.

[33] J.A. Balderas-López, M.R. Jaime-Fonseca, P. Abrica-González, A. Mandelis, On the importance of using reliability criteria in photothermal experiments for accurate thermophysical property measurements, Int. J. Thermophys. 45 (2024) 56, https://doi.org/10.1007/s10765-024-03348-w.

[34] R.R. Naujok, R.V. Duevel, R.M. Corn. Fluorescence and Fourier transform surface-enhanced Raman scattering measurements of methylene blue adsorbed onto a sulfur-modified gold electrode, *Langmuir 9* (1993) 1771–1774. https://doi.org/0743-7463/93/2409-1771$04.00/0.

[35] M. Marchioni, C. Battocchio, Y. Joly, C. Gateau, S. Nappini, I. Pis, P. Delangle, I. Michaud-Soret, A. Deniaud, G. Veronesi, Thiolate-capped silver nanoparticles: discerning direct grafting from sulfidation at the metal–ligand interface by interrogating the sulfur atom, *J. Phys. Chem. C* 124 (2020) 13467–13478, https://doi.org/10.1021/acs.jpcc.0c03388.

[36] R. Matassa, G. Familiari, E. Battaglione, C. Sibilia, G. Leahu, A. Belardini, I. Venditti, L. Fontana, I. Fratoddi, Electron microscopy reveals a soluble hybrid network of individual nanocrystals self-anchored by bifunctional thiol fluorescent bridges, *Nanoscale* 8 (2016) 18161–18169, https://doi.org/10.1039/c6nr06260a.

[37] R. Matassa, S. Orlanducci, G. Reina, M.C. Cassani, M. Passeri, L. Terranova, Structural and morphological peculiarities of hybrid Au/nanodiamond engineered nanostructures, *Sci Rep.* 6 (2016) 31163, https://doi.org/10.1038/srep31163.

[38] F. Ishii, S. Matsunami, M. Shibata, T. Kakuchi, UV-vis absorption study of cis- and trans poly(phenylacetylene)s based on CNDO/S calculation, *Polym. J.* 31 (1999) 84–88, https://doi.org/10.1295/polymj.31.84.

[39] C.W. Lee, K.S. Wong, W.Y. Lam, B.Z. Tang, Light-emitting properties of stereoregular cis-rich poly(phenylacetylene)s, *Chem. Phys. Lett.* 307 (1999) 67–74, https://doi.org/10.1016/S0009-2614(99)00463-7.

[40] M.K. Corbierre, N.S. Cameron, M. Sutton, K. Laaziri, R.B. Lennox, Gold nanoparticle/polymer nanocomposites: dispersion of nanoparticles as a function of capping agent molecular weight and grafting density, *Langmuir* 21 (2005) 6063–6072, https://doi.org/10.1021/la047193e.

[41] A.A. Al-Shamari, A.M. Abdelghany, H. Alnattar, A.H. Oraby, Structural and optical properties of PEO/CMC polymer blend modified with gold nanoparticles synthesized by laser ablation in water, *J. Mater. Res. Technol.* 12 (2021) 1597–1605, https://doi.org/10.1016/j.jmrt.2021.03.050.

[42] O. Trhlíková, J. Zedník, J. Vohlídal, J. Sedláček, Molecular weight and configurational stability of poly(phenylacetylene) prepared with Rh catalyst, *Polym. Degrad. Stab.* 96 (2011) 1310–1320, https://doi.org/10.1016/j.polymdegradstab.2011.04.003.

[43] O. Trhlíková, J. Zedník, J. Vohlídal, J. Sedláček, SEC/DAD and ^{1}H NMR study of molecular weight and configurational stability of poly(2,4-difluorophenylacetylene) and polyphenylacetylene prepared with Rh catalyst, *Macromol. Chem. Phys.* 212 (2011) 1987–1998, https://doi.org/10.1002/macp.201100228.

[44] O. Dammer, B. Vlčková, M. Procházka, D. Bondarev, J. Vohlídal, J. Pfleger, Effect of preparation procedure on the structure, morphology, and optical properties of nanocomposites of poly[2-methoxy-5-(2-ethylhexyloxy)-1,4-phenylenevinylene]

with gold nanoparticles, *Mater. Chem. Phys.* 115 (2009) 352–360, https://doi.org/10.1016/j.matchemphys.2008.12.021.
[45] B. Sun, T. Tao, L. Liu, R. Ding, Y. Mao, Electron transfer facilitated by π–π stacking during the nitrobenzene recognition process of an MOF sensor, *J. Phys. Chem. C* 125 (2021) 12433–12440, https://doi.org/10.1021/acs.jpcc.1c02942.
[46] S. Bhattacharyya, T. Sen, A. Patra, Host–guest energy transfer: semiconducting polymer nanoparticles and Au nanoparticles, *J. Phys. Chem. C* 114 (2010) 11787–11795, https://doi.org/10.1021/jp1030398.
[47] J.-H. Liu, J.-J. Yan, E.-Q. Chen, J.W.Y. Lam, Y.-P. Dong, D.-H. Liang, B.Z. Tang, Chain helicity of a poly(phenylacetylene) with chiral centers between backbone and mesogenic groups on side chains, *Polymer* 49 (2008) 3366–3370, https://doi.org/10.1016/j.polymer.2008.06.007.
[48] E. Davis, N. Mott, Conduction in non-crystalline systems V. Conductivity, optical absorption and photoconductivity in amorphous semiconductors, *Philos. Mag.* 22 (1970) 0903–0922, https://doi.org/10.1080/14786437008221061.
[49] N. Sangiorgi, L. Aversa, R. Tatti, R. Verucchi, A. Sanson, Spectrophotometric method for optical band gap and electronic transitions determination of semiconductor materials, *Opt. Mater.* 64 (2017) 18–25, https://doi.org/10.1016/j.optmat.2016.11.014.
[50] A.H.A. Darwesh, S.B. Aziz, S.A. Hussen, Insights into optical band gap identification in polymer composite films based on PVA with enhanced optical properties: Structural and optical characteristics, *Opt. Mater.* 133 (2022) 113007, https://doi.org/10.1016/j.optmat.2022.113007.
[51] E.T. Kang, A.P. Bhatt, E. Villaroel, W.A. Anderson, P. Ehrlich, Electrical properties of thin films of polyphenylacetylene doped with iodine or arsenic pentafluoride, *Mol. Cryst. Liq. Cryst.* 83 (1982) 307–308, https://doi.org/10.1080/00268948208072180.
[52] Y.-S. Gal, W.-C. Lee, S.-H. Jin, Y.-I. Park, J.-W. Park, K.T. Lim, S.Y. Kim, Electro-optical and electrochemical properties of poly(phenylacetylene), *Mol. Cryst. Liq. Cryst.* 513 (2009) 293–300, https://doi.org/10.1080/15421400903217231.
[53] D. Canto-Reyes, R.A. Soberanis-Ortiz, I. Riech, J.A. Mendez-Gamboa, M. Acosta, Photocurrent enhancement estimation of P3HT:PCBM:Au films as a function of gold nanoparticles concentration, *Gold Bull.* 53 (2020) 141–145, https://doi.org/10.1007/s13404-020-00284-z.
[54] H. Kaçuş, A. Baltakesmez, Z. Çaldıran, Ş. Aydoğan, M. Yılmaz, M. Sevim, Optical and electrical characterization of organic solar cells obtained using gold and silver metal nanoparticles, *Mater. Today Proc.* 46 (2021) 6986–6990, https://doi.org/10.1016/j.matpr.2021.03.276.
[55] P. Aruna, C.M. Joseph, Optical and photosensing properties of gold nanoparticles doped poly (3-hexylthiophene-2, 5-diyl) thin films, *Mater. Lett.* 295 (2021) 129726, https://doi.org/10.1016/j.matlet.2021.129726.
[56] M.O. Farea, A.M. Abdelghany, A.H. Oraby, Optical and dielectric characteristics of polyethylene oxide/sodium alginate-modified gold nanocomposites, RSC Adv. 10 (2020) 37621, https://doi.org/10.1039/d0ra07601e.
[57] S.H. Mejias, E. López-Martínez, M. Fernandez, P. Couleaud, A. Martin-Lasanta, D. Romera, A. Sanchez-Iglesias, S. Casado, M.R. Osorio, J.M. Abad, M.T. González, A.L. Cortajarena, Engineering conductive protein films through nanoscale self-assembly and gold nanoparticles doping, *Nanoscale* 13 (2021) 6772–6779, https://doi.org/10.1039/D1NR00238D.
[58] M. Clausi, M.G. Santonicola, S. Laurenzi, Fabrication of carbon-based nanocomposite films by spin-coating process: An experimental and modeling study of the film thickness, *Compos. A Appl. Sci. Manuf.* 88 (2016) 86–97, https://doi.org/10.1016/j.compositesa.2016.05.026.
[59] Y. Yang, H. Deng, Q. Fu, Recent progress on PEDOT:PSS based polymer blends and composites for flexible electronics and thermoelectric devices, *Mater. Chem. Front.* 4 (2020) 3130–3152, https://doi.org/10.1039/D0QM00308E.
[60] I.K. Backes, L. González-García, A. Holtsch, F. Müller, K. Jacobs, T. Kraus, Molecular origin of electrical conductivity in gold–polythiophene hybrid particle films, *J. Phys. Chem. Lett.* 11 (2020) 10538–10547, https://doi.org/10.1021/acs.jpclett.0c02831.
[61] T. Zhang, Z. Li, K. Li, X. Yang, Flexible pressure sensors with wide linearity range and high sensitivity based on selective laser sintering 3D printing, *Adv. Mater. Technol.* 4 (2019) 1900679, https://doi.org/10.1002/admt.201900679.
[62] A.M. Abdelghany, I.S. Elashmawi, A.A. Al-Shamari, H. Alnattar, Dielectric behavior and AC conductivity of PEO/CMC polymer blend incorporated with gold nanoparticles produced by laser ablation, *J. Mater. Sci. Mater. Electron.* 34 (2023) 388, https://doi.org/10.1007/s10854-022-09797-z.